REVIEW Open Access

Applications of ultrafast nano-spectroscopy and nano-imaging with tip-based microscopy

Zhichen Zhao[1,2], Vasily Kravtsov[3], Zerui Wang[1], Zhou Zhou[1], Linyuan Dou[1], Di Huang[1], Zhanshan Wang[1,2], Xinbin Cheng[1,2*], Markus B. Raschke[4*] and Tao Jiang[1,2*]

Abstract

Innovation in microscopy has often been critical in advancing both fundamental science and technological progress. Notably, the evolution of ultrafast near-field optical nano-spectroscopy and nano-imaging has unlocked the ability to image at spatial scales from nanometers to ångströms and temporal scales from nanoseconds to femtoseconds. This approach revealed a plethora of fascinating light-matter states and quantum phenomena, including various species of polaritons, quantum phases, and complex many-body effects. This review focuses on the working principles and state-of-the-art development of ultrafast tip-enhanced and near-field microscopy, integrating diverse optical pump-probe methods across the terahertz (THz) to ultraviolet (UV) spectral ranges. It highlights their utility in examining a broad range of materials, including two-dimensional (2D), organic molecular, and hybrid materials. The review concludes with a spatio-spectral-temporal comparison of ultrafast nano-imaging techniques, both within already well-defined domains, and offering an outlook on future developments of ultrafast tip-based microscopy and their potential to address a wider range of materials.

1 Introduction

Recent progress in high-resolution optical microscopy has significantly advanced our understanding of key nanoscale physical phenomena, such as polaritons [1–21], moiré physics [22–36], exotic spin textures [37–39], and topological phenomena [40–46]. These breakthroughs enable precise analysis of nanoscale interactions, the impact of defects, and signal heterogeneity, facilitating observations of ultrafast dynamics across nanoscale regions. Such observations reveal critical disparities, deepening our insight into the fundamental mechanisms governing these phenomena. Consequently, developing advanced optical microscopy techniques that offer spatiotemporal resolution beyond intrinsic length scales and dynamic timescales is crucial for characterizing these observations effectively.

For a long time, the spatial resolution has been constrained by the optical diffraction limit in far-field imaging [47]. Although advancements in microscopy have enabled far-field techniques to achieve super-resolution imaging [48], these methods are less suitable for quantum or solid-state materials, as they primarily apply to sparse systems and often require labeling. However, with the emergence of scanning probe microscopy (SPM), it has become possible to go beyond the diffraction limit and achieve spatial resolution at the subwavelength scale. Atomic force microscopy (AFM) [49] and scanning

*Correspondence:
Xinbin Cheng
chengxb@tongji.edu.cn
Markus B. Raschke
markus.raschke@colorado.edu
Tao Jiang
tjiang@tongji.edu.cn
[1] MOE Key Laboratory of Advanced Micro-Structured Materials, Shanghai Frontiers Science Center of Digital Optics, Institute of Precision Optical Engineering, and School of Physics Science and Engineering, Tongji University, Shanghai 200092, China
[2] Shanghai Institute of Intelligent Science and Technology, Tongji University, Shanghai 200092, China
[3] School of Physics and Engineering, ITMO University, Saint Petersburg 197101, Russia
[4] Department of Physics and JILA, University of Colorado, Boulder, CO 80309, USA

tunneling microscopy (STM) [50, 51] are recognized as two fundamental techniques in the SPM, renowned for their ability to achieve atomic-scale spatial resolution through the utilization of a tip. The subwavelength structure of the tip apex enables near-field localization of light, achieving optical spatial resolution in the nanometer range and effectively overcoming the spatial averaging effects typically encountered in the far field. The breakthrough has further inspired the invention of various tip-based SPM techniques. Owing to its fundamental compatibility with optical techniques, the advancement has led to the development of scanning near-field optical microscopy (SNOM) [52–54], tip-enhanced Raman spectroscopy (TERS) [55–60], nanoscale Fourier transform infrared spectroscopy (nano-FTIR) [61], thermal infrared nano-spectroscopy (TINS) [62–65], synchrotron infrared nano-spectroscopy (SINS) [66–68], and others. Building on the various SPM techniques capable of breaking the diffraction limit, further integration with ultrafast techniques has enabled the simultaneous achievement of high spatial and temporal resolutions [69–72]. As shown in Fig. 1a, the tip apex, being a subwavelength structure, provides spatial resolution comparable to its size. By adjusting the time delay between the pump and probe pulses that illuminate the tip, time-resolved experiments can be conducted. The temporal resolution is mainly related to the precision of the time delay control and the pulse duration. Notably, in ultrafast tip-based experiments, samples are often subjected to thermal effects and photodamage resulting from laser irradiation, particularly when high-intensity femtosecond pulses are utilized. To minimize these effects, various approaches can be employed. An effective approach involves reducing the laser power or adjusting the pulse duration to limit heat accumulation in the sample [73]. Additionally, applying cryogenic techniques during experiments can significantly decrease photodamage. This integration enables real-time observation of electronic, vibrational and magnetic dynamics at the nanoscale, which advances the exploration of ultrafast interaction processes

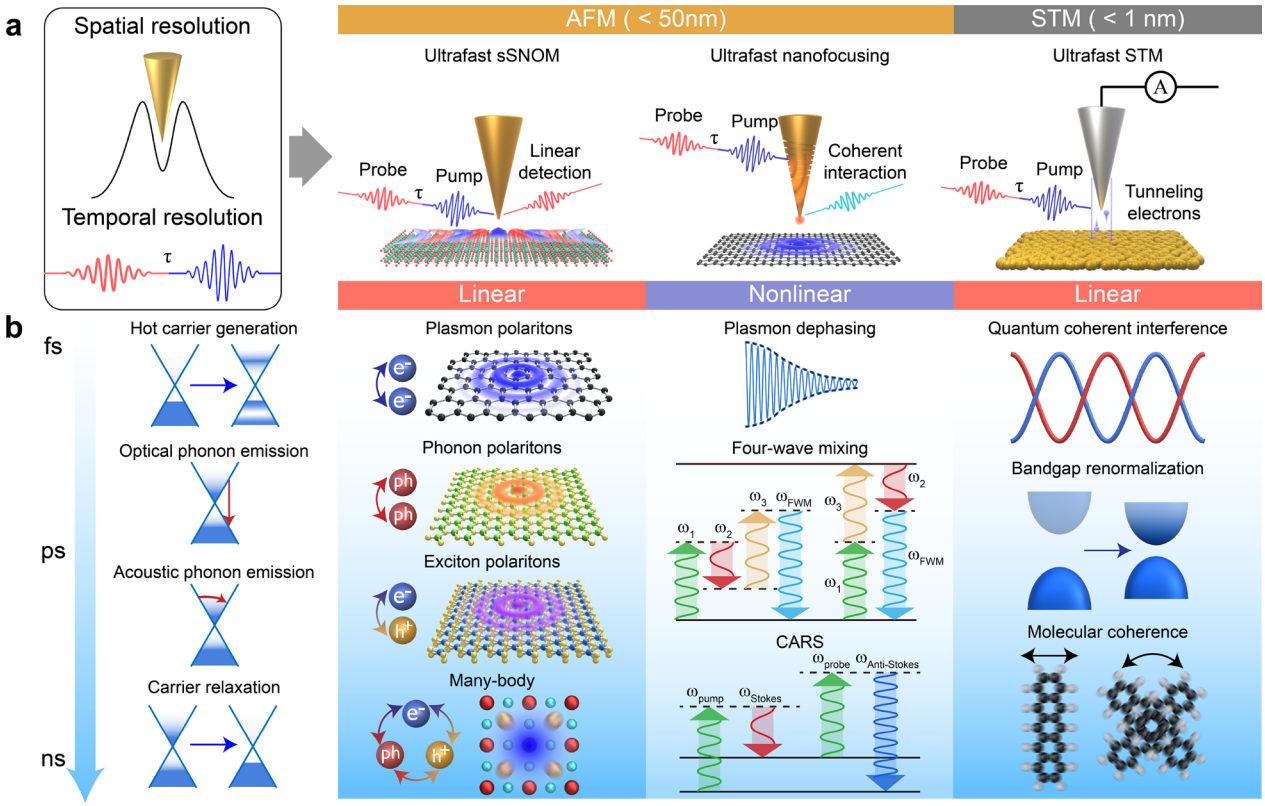

Fig. 1 Ultrafast nano-spectroscopy and nano-imaging. **a** The combination of scanning probe microscopy and optical pump-probe spectroscopies enables simultaneous access to spatial and temporal resolutions. Both ultrafast *s*-SNOM and ultrafast nanofocusing are based on AFM with a spatial resolution comparable to the size of the tip, typically on the order of tens of nanometers. The former is effective in detecting light-matter interactions in linear optical regime, while the latter enables the investigation of coherent phenomena through grating-tip coupling in nonlinear optical regime. Ultrafast STM can provide subnanometer-scale spatial resolution by relying on the tunneling processes occurring in the STM junction. **b** Exploration of physical processes through the above spatiotemporally resolved techniques, sorted on the basis of their characteristic times. The left panel displays time scales dominated by different interactions for reference

characterized by ultrashort lifetimes ranging from femtosecond to nanosecond time scales.

In this review, we concentrate on three types of ultrafast microscopy techniques: ultrafast scattering-type scanning near-field optical microscopy (ultrafast *s*-SNOM), ultrafast nanofocusing, and ultrafast STM (Fig. 1a). The spatial resolution of *s*-SNOM is primarily determined by the dimensions of the tip apex [74]. Compared to aperture-type SNOM, another significant branch of SNOM where smaller apertures compromise signal strength due to the waveguide cutoff effect, *s*-SNOM does not suffer from this limitation [74]. Consequently, *s*-SNOM has been more widely developed and utilized in recent years. By combining with the optical ultrafast techniques, *s*-SNOM provides a powerful tool for investigating the ultrafast dynamics of phenomena in linear optical regime, compatible with a broad range of optical wavelengths and working temperatures [75–77]. To extend the research into the nonlinear optical regime, plasmonic nanofocusing on a metal tip has been developed. Ultrafast nanofocusing not only enables detection of nonlinear effects such as second-harmonic generation (SHG) [78–80], four-wave mixing (FWM) [80–82], and coherent anti-Stokes Raman scattering (CARS) [83], but its coherent detection also allows for the characterization of important physical processes such as electronic dephasing. Compared with these two AFM-based techniques, ultrafast STM can achieve sub-ångström spatial resolution in a low-temperature vacuum environment. Ultrafast STM grounded in the principles of electron tunneling enables the study of electronic and vibrational dynamics at the atomic scale. Figure 1b presents a summary of significant physical phenomena investigated via tip-based ultrafast microscopy in various materials, including 2D materials, molecules, metals, and perovskites, categorized by their characteristic lifetimes, as discussed in this review.

The structure of this review is as follows: The first part discusses nano-imaging and nano-spectroscopy using ultrafast *s*-SNOM, including the characterization of spatial heterogeneity and polariton propagation, and spectral analysis under weak and strong perturbation conditions. The second part provides an overview of the development and significant contributions of ultrafast nano-spectroscopy and nano-imaging using nanofocusing techniques, and also covers nanofocusing-based ultrafast electron microscopy, such as the ultrafast point-projection electron microscopy (UPEM). The final part deals with various lightwave modulation methods applied in ultrafast STM and explores the development in coherent manipulation of electrons. The review concludes with a summary of current advancements and challenges, and provides an outlook on the potential future developments in the field of ultrafast tip-based microscopy. Therefore, we expect that this review will equip readers with a systematic understanding of this field while also inspiring researchers to gain more diverse insights for technical innovation.

2 Ultrafast *s*-SNOM

Ultrafast *s*-SNOM is a noninvasive and versatile technique capable of probing carrier and lattice dynamics in various materials with high spatial and temporal resolution, as shown in Fig. 1. For the selection of a material system for ultrafast *s*-SNOM research, key considerations include but are not limited to, optical properties and structural characteristics. Materials with optical resonant modes are particularly suitable for investigating light-matter interactions, including polaritons [84–92], polarons [93–95], quantum phases [73, 96–98], and a range of many-body phenomena. For example, 2D materials, phase change materials, and perovskites are ideal candidates for studying photoinduced processes. Additionally, this technique holds promise for exploring novel structures such as superlattices [99], nanowires [100, 101], and nanotubes [102]. The precision of ultrafast *s*-SNOM in analyzing various excitation dynamics is instrumental in advancing our understanding and control of specific physical phenomena within these materials at the nanoscale.

Figure 2a presents an early example of ultrafast *s*-SNOM demonstrated in 2014 [84]. This *s*-SNOM configuration consists of a Michelson interferometer combined with a tapping-mode AFM. The AFM tip, featuring a radius of tens of nanometers, provides a large momentum range on the order of the inverse of its radius of curvature and local field enhancement, enabling the investigation of physical phenomena with momentum surpassing that of free-space light and delivering nanoscale spatial resolution. To further achieve ultrafast temporal resolution, ultrashort pulses are used as pump and probe pulses. Precise control and calibration of the optical pump-probe method are essential to ensure experimental success. Accurate synchronization of the pump and probe is necessary to achieve optimal temporal resolution. This can be accomplished using a mechanical stage that controls the time delay of the pulses, allowing for precise adjustments to the temporal overlap between the pump and probe. Additionally, minimizing mechanical and thermal drift is crucial, as these factors can affect the alignment and timing of the pump-probe pulses. Active stabilization systems are commonly employed to maintain stability during measurements. The pump pulses induce a ground state perturbation. Demodulating the probe pulse signal at high harmonics of the tip tapping frequency enables the acquisition of temporally

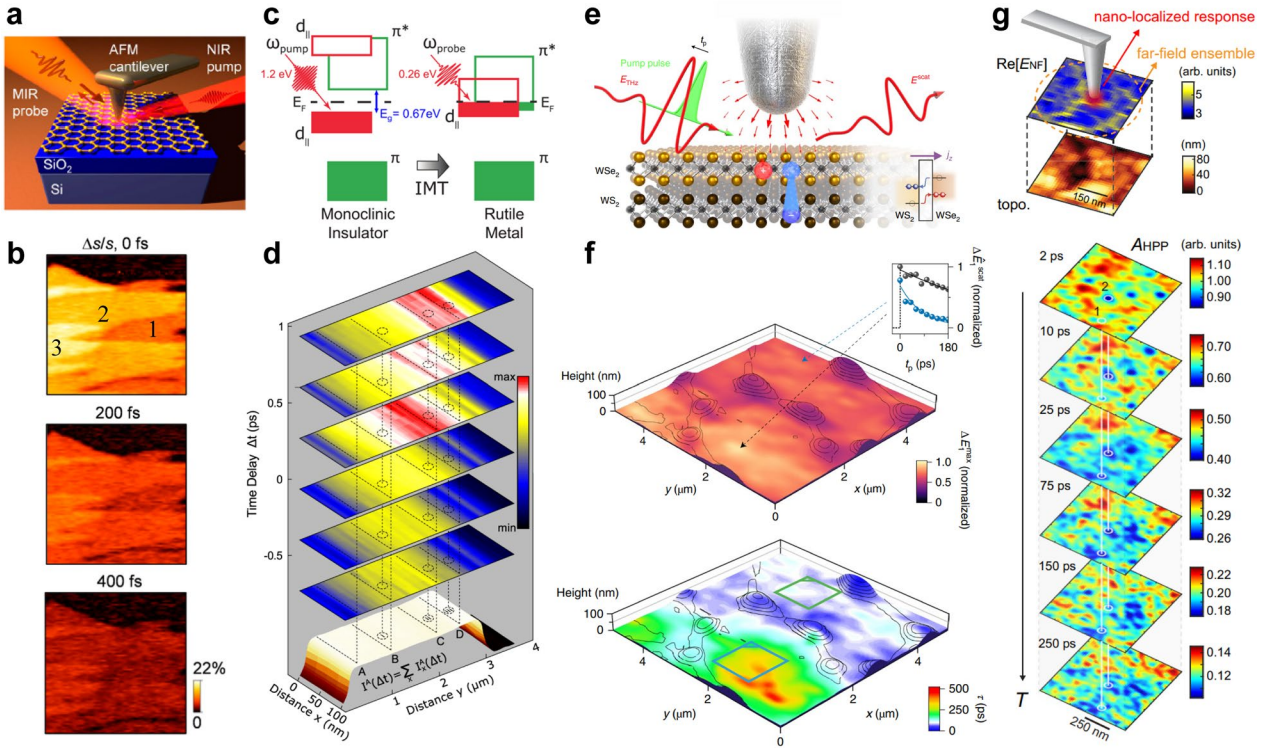

Fig. 2 Nanoscale heterogeneity revealed by ultrafast nano-imaging. **a** Schematic of ultrafast NIR-pump/MIR-probe *s*-SNOM on exfoliated graphene. **b** Spatiotemporally resolved *s*-SNOM images of exfoliated graphene. **c** Electronic band structure diagram for NIR-pump/MIR-probe response of IMT in VO_2. **d** Spatiotemporally resolved *s*-SNOM images with far-from-equilibrium excitation of IMT dynamics of a VO_2 microcrystal. **e** Schematic of ultrafast visible-pump/THz-probe *s*-SNOM experiment on WSe_2/WS_2 heterostructure. Inset is the band diagram for the carrier tunneling occurred at the gap. **f** Spatially resolved *s*-SNOM image (top panel) and decay time image (bottom panel) combined with black contour lines. Inset shows the electric field intensity measured on two flat regions. **g** Schematic of ultrafast visible-pump/MIR probe *s*-SNOM experiment on triple cation perovskites (top panel). Spatiotemporally resolved images of photoinduced carrier dynamics (bottom panel)

resolved near-field amplitude and phase measurements influenced by pump excitation [103, 104], and allows for the extraction of near-field spectra from interferograms through nano-FTIR.

2.1 Ultrafast nano-imaging of spatial heterogeneity

To unravel the complex and heterogeneous dynamics of physical phenomena at the nanoscale, ultrafast *s*-SNOM offers unprecedented insights through nano-imaging. In the early example depicted in Fig. 2a, the integration of near-infrared (NIR) pump and mid-infrared (MIR) probe spectroscopy with *s*-SNOM was employed to probe the ultrafast dynamics of Dirac plasmons in graphene, achieving an analysis at temporal and spatial resolutions of 200 fs and 20 nm, respectively [84]. The near-field response of this sample originates from the interaction between graphene plasmons and the surface phonon modes of SiO_2. Figure 2b displays spatiotemporally resolved near-field mapping of a region containing various layers of graphene exfoliated on a SiO_2/Si substrate, with the number of layers indicated in the top panel and confirmed by Raman spectroscopy. Results of spatiotemporal mapping uncover significant heterogeneity in the evolution of the near-field plasmonic response of graphene corresponding to the number of layers. Decay times associated with various layer numbers can also be extracted, quantitatively revealing the dynamics of interactions between hot carriers and phonons. In another implementation, THz nano-imaging of a gold grating embedded in a Si_3N_4 layer by integrating *s*-SNOM with THz pulses was achieved, demonstrating its subsurface near-field nano-imaging capabilities [105]. THz response of graphene and phase-resolved THz nano-imaging of WTe_2 were further explored, respectively, exhibiting phenomena different from observations at infrared frequencies due to low-energy excitations [106, 107].

While the experiments above were generally performed with weak pump excitations leading to a weak ground state perturbation, the use of intense amplified laser pulses allows for the far-from-equilibrium and significant excited-state pumping. This enabled ultrafast *s*-SNOM to be utilized to investigate the dynamics of

the photoinduced insulator-to-metal transition (IMT) in vanadium dioxide (VO_2) [73, 95, 97, 108]. Pump pulses with energy above the band gap are used to induce IMT, while MIR probe pulses are used to observe the near-field Drude response of the emergent metallic phase of VO_2 (Fig. 2c). Figure 2d shows a series of temporally resolved *s*-SNOM maps of a VO_2 microcrystal, revealing the photoinduced collapse of the band structure and the emergence of the metallic phase on sub-picosecond time scales. It was shown that the region with a strong near-field response shifts over time from the middle of the crystal toward the edge. These time-resolved images reveal the temporal progression of nanoscale heterogeneity during photoinduced IMT in the VO_2 microcrystal. In related experiments, albeit at low pump fluences and contributions of the thermally induced IMT pathways, the dynamics of IMT in VO_2 nanobeams [109] and thin films [98] were investigated. These studies focused on the relationships between heterogeneity in IMT dynamics and varying pump intensity, ambient temperature, and nucleation sites.

Besides the studies on homostructures discussed above, ultrafast *s*-SNOM enables detailed exploration of the dynamics of local polarizability in heterostructures [110, 111]. Using a combination of *s*-SNOM with THz probe pulses, the dynamics of charge transfer associated with electron–hole pairs in the transition metal dichalcogenide (TMD) heterostructures were resolved (Fig. 2e). The WSe_2/WS_2 heterobilayer exhibits type-II band alignment, facilitating the separation of photoinduced electrons and holes into different layers. In this heterostructure, the interlayer tunneling process has the capability to generate coherent THz emission [112]. Consequently, the density of interlayer electron–hole pairs can be quantified through the detection of the THz emission electric field. Figure 2f overlays the 3D topography with near-field amplitude (top panel) and the decay time of the photoinduced carriers (bottom panel). The heterogeneity in these mappings reflects the distribution of the density of electron–hole pairs. This work also provides a novel approach to investigate the tunneling process without monitoring the lightwave-driven current.

To further reveal the intricate many-body carrier dynamics, ultrafast *s*-SNOM can also be used to investigate the complex interplay involving electron–phonon interactions and electron–electron interactions [93–95]. To achieve the necessary combination of strong pump far-from-equilibrium excitation with selectively probing the excited state, an ultrafast heterodyne pump-probe system was developed [95]. This approach allows visualization of the spatiotemporal evolution of the photoinduced carrier absorption in a triple cation perovskite by capturing ultrafast "movies" (Fig. 2g). The application of the phenomenological adiabatic polaron absorption model and conventional Drude model allowed to extract the carrier relaxation rate from these spatiotemporally resolved mappings. The analysis suggests that the heterogeneity observed in the transient absorption of the triple cation perovskite can be attributed to variations in the interaction between photoinduced carriers and the perovskite lattice.

2.2 Ultrafast nano-imaging of polariton propagation

Polaritons, as half-light half-matter quasiparticles emerging from the coupling of electromagnetic waves with material excitations, have become a promising pathway for manipulating light at the nanoscale. Polaritons are of great significance in exploring the properties and functions of materials due to their ability to confine electromagnetic waves to dimensions much smaller than the wavelength of light. This confinement enhances light-matter interactions, revealing material-specific electron dynamics, vibrational modes, and optical responses that are difficult to achieve through other techniques. Furthermore, polaritons allow probing of anisotropic properties in low-dimensional materials, as well as the coupling between electronic, vibrational, and optical excitations, making them indispensable in both fundamental and applied research of materials. In past studies, infrared *s*-SNOM has been successfully employed to image the real-space interference patterns of polaritons, which can be tuned by varying the gate voltage applied to the graphene [113–117]. By combining with polariton interferometry measurements, ultrafast *s*-SNOM enables observation of the polariton propagation and interference simultaneously in space and time. It is noteworthy that polaritons with either near-zero group velocity or high propagating loss cannot be detected by *s*-SNOM, due to the absence of polariton interference.

In application to the phonon polaritons (PhPs), ultraslow PhPs in a thin hexagonal boron nitride (h-BN) slab, which supports two types of hyperbolic PhPs at 760–825 cm^{-1} (HPI) and 1370–1610 cm^{-1} (HPII), were respectively observed [85]. Figure 3a shows the near-field fringes originating from the interference between the edge-launched propagating polaritons and tip-reflected propagating polaritons. By adjusting the time delay of incident pulses (~100 fs duration) and subtracting the background signal, the propagation of PhPs was visualized with nanometer and femtosecond resolution in the HPII spectral range (Fig. 3b). E_{dir} represents the light directly scattered by the tip at zero time delay. The evolution of E_{HP} shows the PhPs launched by the gold film propagating in time. The lifetime of hyperbolic PhPs and the signs of group and phase velocities can be extracted from these time-resolved data. As shown in Fig. 3c, the

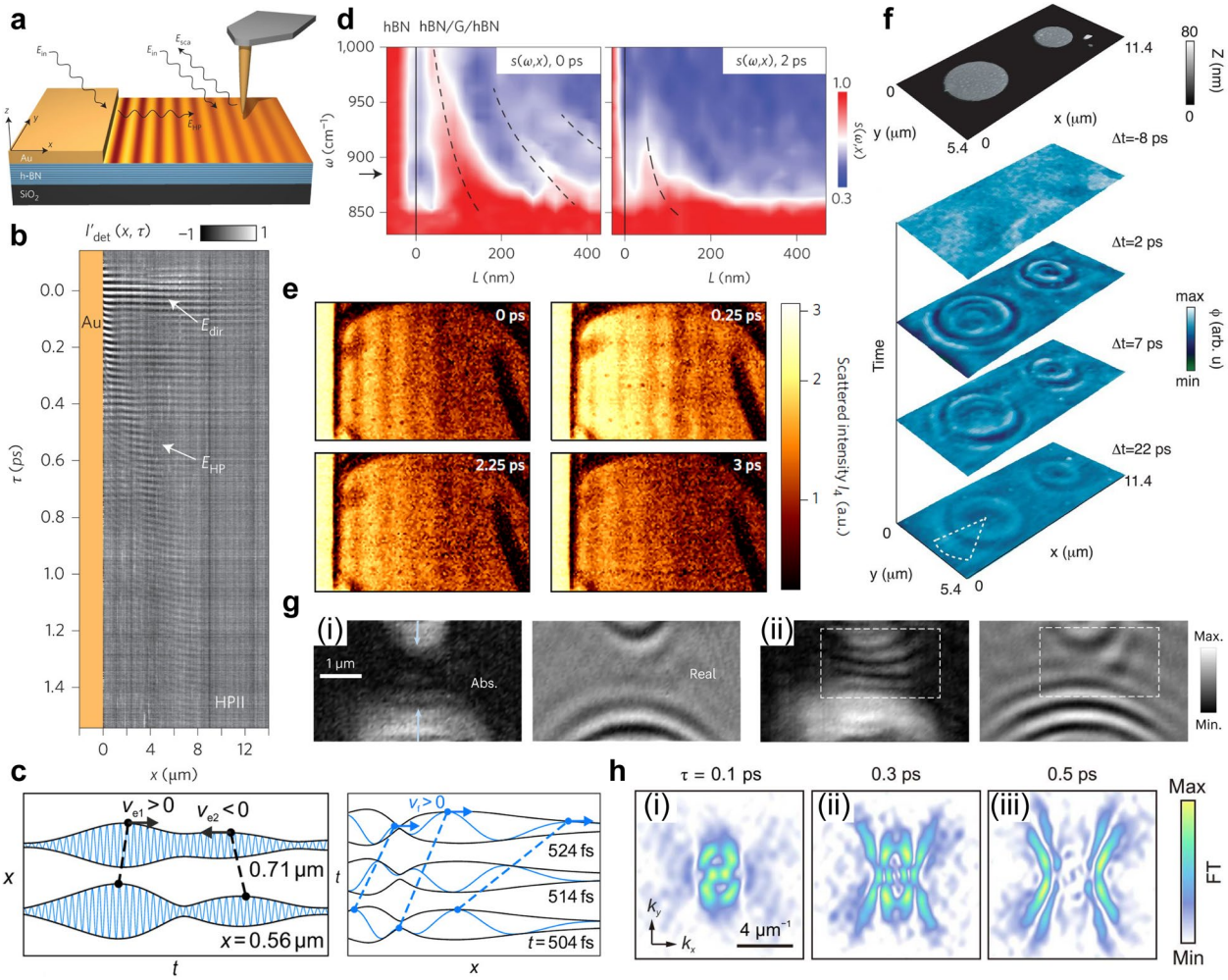

Fig. 3 Ultrafast dynamics of polariton propagation in polaritonic materials. **a** Schematic of ultrafast MIR-pump/MIR-probe *s*-SNOM experiment on Au/h-BN/SiO_2 system, supporting PhPs launched at the edge of gold film. **b** Ultrafast dynamics of PhPs, unveiled by the evolution of scattered electric field intensity versus distance from the gold edge in the HPII spectral range. **c** Near-field signal of PhPs obtained at fixed spatial positions and time delays, with V_e (left panel) and V_f (right panel) representing the envelope velocity and fringe velocity, respectively. **d** Ultrafast dynamics of plasmon polaritons, as indicated by the spectra measured at different delay times versus the distance from the graphene edge. The dashed lines mark the positions where the spatial derivative of $s(\omega, x)$ with respect to x, $ds(\omega, x)/dx = 0$. **e** Ultrafast dynamics of hybrid phonon-plasmon polaritons, demonstrated through spatiotemporally resolved images of scattered electric field intensity measured on SiO_2/BP/SiO_2 system. **f** Topograhic image of WSe_2 slab on two gold antennas (top panel). Ultrafast dynamics of hyperbolic exciton-polaritons, captured through spatiotemporally resolved images of optical phase in the region corresponding to the top panel (bottom panel). **g** (i) The amplitude (left panel) and real part (right panel) of the near-field interference of PhPs launched by two gold antennas on α-MoO_3 flake at 990 cm^{-1}, measured at 11.14 ps. (ii) The corresponding measurements at a complex frequency of (990 - 2i) cm^{-1}. **h** Evolution of isofrequency contours extracted from ultrafast *s*-SNOM measurements, revealing the topological transition from lenticular to hyperbolic

opposite signs of the envelope velocities V_{e1} and V_{e2} derived from the near-field fringes reveal the coexistence of both positive and negative group velocities, and the fringe velocity V_f indicates positive phase velocity in the propagation of PhPs [118].

Meanwhile, the presence of surface plasmon polaritons (SPPs) in graphene can be dynamically monitored [86], e.g., the generation and propagation of SPPs in a single-layer graphene encapsulated in h-BN (Fig. 3d). Through the photoinduced increase in carrier density, the interference fringes became clearly visible, with standing waves arising from the interference between tip-launched and edge-reflected SPPs. Nano-FTIR measurements on graphene then capture near-field hyperspectral images as a function of time delay and distance between the tip and the graphene edge. In addition, the dispersion of SPPs can be analyzed by converting the distance into momentum. Clearly, the period of standing waves decreases as

the frequency increases, reflecting plasmonic dispersion with a positive group velocity. There is an obvious reduction in both the period and signal strength over delay time, which can be attributed to the relaxation of hot carriers.

Further, hybrid polaritons which arise from the coupling of plasmon [86], phonon [85], and exciton polaritons [87, 88] can be spatiotemporally imaged. Near-field nano-imaging and nano-FTIR have resolved the switching and decay of hybrid polaritons in a SiO_2/black phosphorus (BP)/SiO_2 heterostructure [89] (Fig. 3e). The BP supports SPPs that can couple with phonons within the Reststrahlen band of SiO_2. In contrast to the behavior of SPPs in graphene, the period of the hybrid polaritons shows no significant changes with time delay, while the propagation length increases due to the involvement of phonons. This behavior of the period and propagation length provides evidence of the coupling between the SPPs and the phonons, in agreement with theoretical expectations.

To comprehensively investigate the topological properties of polaritons, ultrafast *s*-SNOM can enable the visualization of polaritons in 2D materials in both real space and k-space by employing nanoantennas such as metal disks [90–92]. Different from the direct observation of the propagation of exciton polaritons [87], the pump-induced out-of-plane hyperbolic dispersion of exciton polaritons was investigated in a configuration with a gold disk placed underneath the WSe_2 slab [91]. The temporal variations of the interference fringes can be clearly observed (Fig. 3f). The dispersion of polaritons is associated with the density of the electron–hole pairs generated by the pump pulses, which allows for pump intensity control of the near-field patterns and analysis of hyperbolic Rydberg polaritons. Similarly, in-plane anisotropic polaritons can also be monitored in spatiotemporal nano-imaging by placing a gold disk on the surface of polaritonic materials [92, 119]. The interference of in-plane hyperbolic PhPs launched by two gold antennas on the α-MoO_3 film was investigated at 990 cm^{-1} (Fig. 3g-(i)). However, the interference was weak due to the attenuation of polaritons during propagation. To compensate for intrinsic losses in polariton propagation, a multifrequency approach was demonstrated to synthesize the complex-frequency wave (CFW) [119–121]. Utilizing the CFW excitation, the propagation distance of the polaritons was significantly increased, as confirmed by the enhanced interference at (990-2i) cm^{-1} (Fig. 3g-(ii)). With the emergence of polaritons with diverse topological properties, such as shear [18], ghost [15], and canalized [122] polaritons, analyzing topological transitions in k-space has become essential. As shown in Fig. 3h, by applying 2D Fourier transform to real-space images, the shape of isofrequency contours (IFCs) was observed to change over time from lenticular to hyperbolic, directly revealing the dynamic evolution of polariton dispersion in anisotropic material.

2.3 Spatiotemporally resolved nano-spectroscopy

Previous sections introduced ultrafast *s*-SNOM experiments probing heterogeneities in material responses in spatiotemporal nano-imaging. The experiments shown so far detected the probe signal in a spectrally integrated fashion, i.e., without spectroscopic information. In order to also obtain information about the electronic or lattice resonances, time-resolved nano-spectroscopy or full spatio-spectral-temporally resolved nano-imaging needs to be performed. Ultrafast nano-spectroscopy implements time-resolved spectroscopy with nanoscale spatial resolution [123], which is essential to investigate the underlying mechanisms responsible for the heterogeneity arising from various interaction processes in different materials and systems, including graphene [124], semiconductors [99, 125], plasmonic nanostructures [100], and others.

The dynamics of various light-matter interactions investigated through ultrafast nano-spectroscopy can be broadly categorized into two parts: short-lived excited states under weak perturbation and long-lived excited states under strong perturbation. Figure 4a illustrates the mechanism of short-lived excited states in the narrow bandgap semiconductor InAs [124]. The NIR pulse is used to pump carriers across the bandgap, while the MIR pulse is utilized to probe the near-field time-resolved spectra during the generation of hot carriers and subsequent relaxation. Nano-spectroscopy has been employed to investigate the dynamics of pump-induced changes to the surface plasmons in an InAs film ($\sim$2 μm) grown on a GaAs substrate with 200 fs temporal resolution [124]. Similarly, Fig. 4b provides an example of NIR pump/THz probe spectra measured on an InAs nanowire [126]. In this study, electro-optic sampling was used for subcycle gate pulse (<10 fs) detection, achieving 10 nm spatial resolution and 10 fs temporal resolution. The solid blue line indicates the evolution of the resonance frequency over the pump-gate delay time, providing insight into the carrier density variation in the nanowire.

In the application to photovoltaic perovskites and in extension to the ultrafast *s*-SNOM of the polaron dynamics with far-from-equilibrium excitation [94, 95], spectrally resolved heterodyne detected ultrafast *s*-SNOM was performed. Figure 4c shows the diagram of the pump-probe measurement concerning long-lived excited states with strong perturbation, depicting the process of the spectrally resolved extraction of the excited state lattice vibration in the form of the complex dielectric response. The pump-induced excited-state carriers give

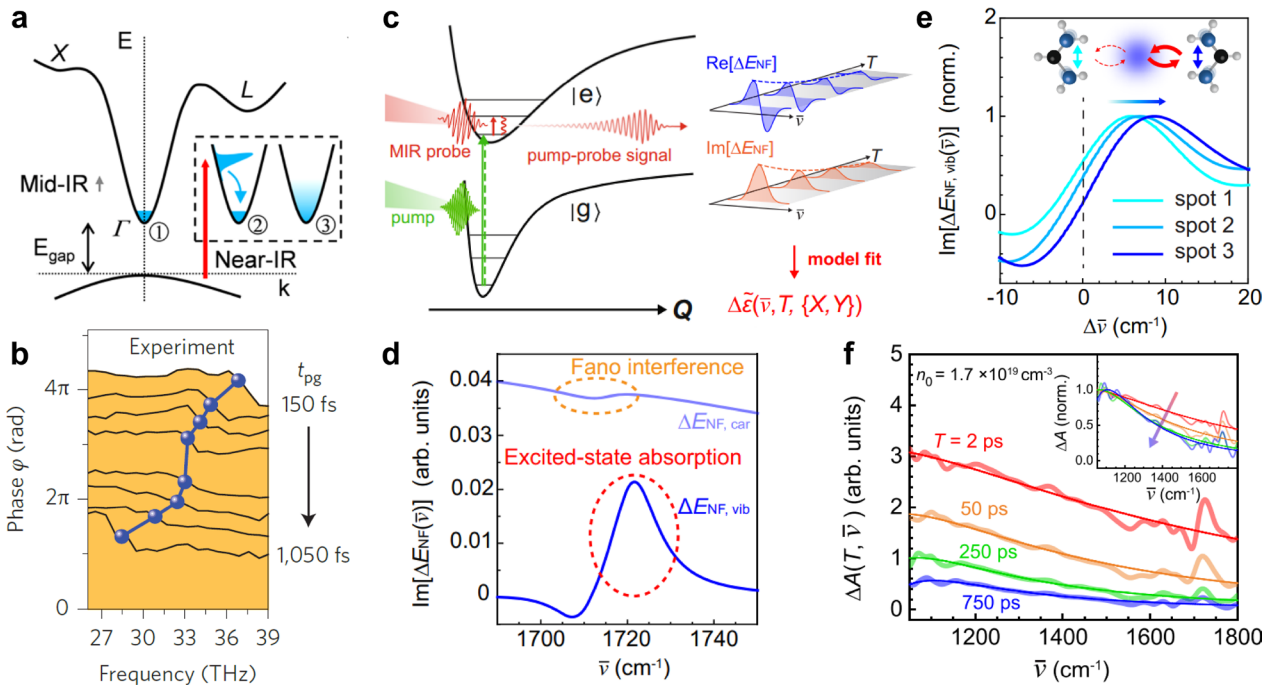

Fig. 4 Ultrafast nano-spectroscopy with s-SNOM. **a** Schematic of the InAs band structure. Inset depicts carrier generation and the Fermi-Dirac distribution before relaxation to the equilibrium state. **b** Temporally resolved absolute phase spectra of the scattered electric field, measured at the center of the InAs nanowire. **c** Schematic illustrating the procedure for retrieving the dielectric function change from the pump-probe signal. **d** Composition analysis of Im[ΔE_{NF}], showing separated contributions from vibrational and carrier responses. **e** Spatial heterogeneity in polaron-cation coupling revealed by measurements at different positions on the perovskite. **f** Temporal evolution of absorption spectra of the perovskite

rise to both a soft lattice (polaron) response and modification of the molecular cation vibration. The temporally resolved complex spectral profile $\triangle E_{NF}$ of the near-field MIR signal can be extracted from the collected pump-probe signal by the Fourier transform. The pump-induced change with respect to the ground state in the complex spectral profile in lead halide perovskites resolves the spatial heterogeneity in the coupled electron-lattice-molecular cation response. The derived frequency shift of the Im[$\triangle E_{NF}$] comprising contributions from both Fano-type interference and excited-state vibrational absorption, is consistent with the polaron-cation coupling. The distinct contributions of vibrational and carrier responses to spectral change are able to be identified separately (Fig. 4d). In Fig. 4e and f, spectral profiles were acquired at different locations and delay times on the perovskite film, respectively. The different vibrational frequency shifts of Im[$\triangle E_{NF}$] reveal the spatial heterogeneity in the polaron-cation coupling, which cannot be detected by far-field spectroscopy because of spatial averaging. The narrowing of transient absorption spectra with increasing time delay is interpreted as progressive carrier stabilization, attributable to mechanisms such as polaron formation, revealing the photoinduced polaron dynamics. Recently, the dynamics of charge carriers in organic–inorganic metal halide perovskite films have also been studied through ultrafast *s*-SNOM implementing THz nano-spectroscopy with subcycle temporal resolution, which facilitates the analysis of chemical composition and crystallographic phase [127]. These results provide a real-space real-time view of the spatio-spectral-temporal dynamics underlying the photophysical response of perovskites.

3 Ultrafast nanofocusing

Traditional near-field optical microscopy provides a versatile tool for ultrafast nano-imaging in the linear optical regime. However, advanced ultrafast spectroscopic techniques such as coherent 2D spectroscopy, which can probe coupled degrees of freedom and coherent dynamics of various excitations in matter, require nonlinear optical signals. Generating near-field coherent nonlinear optical responses in *s*-SNOM is challenging due to the generally weak local field enhancement and lack of synchronization between cantilever oscillations and pulsed laser output in terms of repetition rate and duty cycle. Recently, an alternative approach to coherent nonlinear nano-spectroscopy and nano-imaging has

been developed. This approach is based on the concept of adiabatic plasmonic nanofocusing [128, 129], which is schematically illustrated in Fig. 1a and further demonstrated in Fig. 5a. Another innovative method involves designing a spiral-grating metal-coated tip on an optical fiber, which enables high resolution while maintaining high throughput and contrast [130] (Fig. 5b). Instead of focusing onto the apex of a tip as in conventional near-field optical microscopy, the incident light is first coupled into SPPs away from the tip apex, for example, via a grating coupler. The SPPs then propagate without radiation into the far field on the surface of a tapered tip towards the apex. Upon propagation, the lowest-order azimuthal mode experiences a continuous asymptotic increase of the group index, 3D mode compression, slow down [131], and field enhancement, eventually scattering into the far field at the apex [132]. As a result, a bright point-like light source is formed at the tip apex, which can be used for background-free nano-spectroscopy and nano-imaging.

3.1 Nanofocusing-based ultrafast nano-spectroscopy and nano-imaging

Among various experimental implementations of adiabatic plasmonic nanofocusing, the conical metal tip

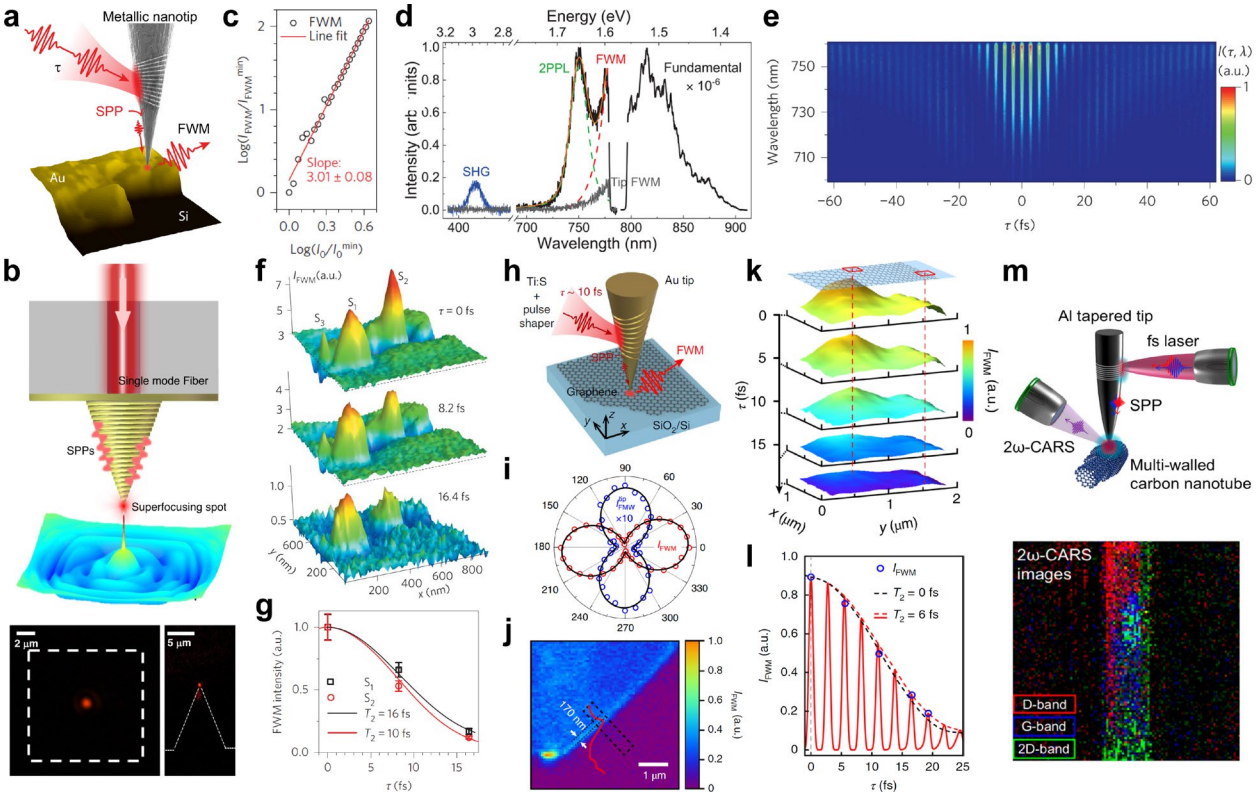

Fig. 5 Femtosecond nanofocusing and nonlinear nano-imaging. **a** Schematic illustration of ultrafast SPP nanofocusing on a sharp metal tip brought into close proximity to sample surface. **b** Schematic of a spiral-grating conical tip integrated on an optical fiber for nanofocusing measurements (top panel). Top and side views of the optical nanofocusing spot emitted from the tip apex (bottom panels). **c** Power dependence of nanofocused FWM signal on a log-log scale (circles), with a cubic fit (red line) showing slope of 3.01 ± 0.08. **d** Nanofocused FWM and fundamental SPP spectra collected from the tip apex in proximity with WSe_2 monolayer. **e** Interferometric FWM spectrogram measured on a bare tip. **f** Nanofocused FWM images measured on a gold step edge with two-pulse excitation, corresponding to an inter-pulse delay of τ = 0 fs (top), 8.2 fs (middle) and 16.4 fs (bottom) and demonstrating evolution of the relative intensities in spots S_1, S_2 and S_3. **g** FWM intensity in S_1 and S_2 for 3 selected delays, showing variation in dephasing time T_2, with simulation for T_2 = 16 fs (black curve) and T_2 = 10 fs (red curve). **h** Schematic of grating-coupling and femtosecond adiabatic nanofocusing combined with pulse shaping for nanolocalized FWM excitation in graphene. **i** Normalized polarization dependence of graphene FWM (red) and tip FWM (blue, magnified x10), fitted by a $\cos^2\theta$ dependence. **j** Nanofocused FWM imaging of monolayer graphene with a line-cut (red) extracted from signal averaging along the edge-parallel direction (across the rectangular box). **k** FWM images of graphene with two-pulse excitation, corresponding to five inter-pulse delays (from top to bottom), τ = 0, 5.6, 11.2, 16.6 and 19.3 fs. **l** FWM intensity of the graphene edge (right red square in **k**) for 5 selected delays (blue circles), with finite decoherence time of T_2 = 6 ± 1fs (red solid curve and red dashed envelope), compared to a simulated instantaneous response (black dashed envelope). **m** Schematic of nanofocusing-based 2ω-CARS measurement on the multi-walled carbon nanotube (top panel). Nanofocusing-based 2ω-CARS imaging at the D-, G-, and 2D-bands (bottom panel)

geometry with a grating engraved at a 10–30 μm distance from the tip apex [133] has proved particularly suitable for ultrafast nano-spectroscopy as it is intrinsically broadband, compatible with ultrashort laser pulses, and can be easily incorporated into a scanning probe microscope, for example, in the non-contact shear-force feedback mode. For time-resolved spectroscopy with few-fs temporal resolution, ultrashort laser pulses are spectrally shaped, grating-coupled, and nanofocused on a tip. In order to achieve transform-limited pulses at the tip apex, dispersion pre-compensation and pulse shaping [79, 134, 135] have been used together with adaptive iterative algorithms such as multiphoton intra-pulse interference phase scan (MIIPS). The feedback signal for optimizing the pulse shape is provided by local SHG, which results from the broken inversion symmetry in the axial direction [136] and nanofocusing-induced compression of the SPP mode volume with multi-fold increase in the local optical field amplitude at the tip apex. Further, full deterministic optical waveform control of nanofocused SPPs has been enabled as demonstrated in [79] via measurements based on frequency-resolved optical gating (FROG and XFROG).

The nanofocusing approach enables simultaneous compression of optical fields in space and time. Experiments on imaging nanostructured surfaces [137] and nanoparticles [138] with nanofocused SPPs have demonstrated field localization at the sub 20–30 nm level, which can be improved further to a few-nm level by using the gap-plasmon geometry [139]. This allows various implementations of nanofocusing-based imaging of nanomaterials with deep subwavelength spatial resolution, as demonstrated in several works with nano-localized Raman spectroscopy [140, 141], photocurrent imaging [142], coherent light scattering [143], and broadband spectral bandgap nano-imaging [144]. In the temporal domain, the nanofocused SPP pulse durations can reach down to the few-cycle level limited by the employed laser sources, as has been demonstrated in experiments on nanofocused photoemission [145, 146], enabling the implementation of nanofocusing-based ultrafast spectroscopy via spectral interferometry [147] and local manipulation of low-dimensional materials with femtosecond laser pulses [148].

The nm-fs spatiotemporal confinement of optical fields achieved with adiabatic plasmonic nanofocusing opens new opportunities for generating nonlinear optical signals on the nanoscale. Particularly interesting are third-order nonlinear processes, which provide the basis for all-optical control and enable realization of multidimensional spectroscopies for studying quantum coherence and coupling in nanomaterials. Efficient third-order nonlinearity has been demonstrated for SPPs nanofocused on a gold tip via FWM [81]. In the experiment, the FWM response is generated predominantly within the nanoscopic volume at the apex and exhibits a cubic dependence on the excitation power as shown in Fig. 5c. The short-wavelength part of a broadband excitation laser spectrum is blocked with a long-pass filter, and the FWM signal is selected with a short-pass filter resulting in fundamental and FWM spectra shown in Fig. 5d. A two-pulse interferometric FWM spectrogram illustrated in Fig. 5e can be used to probe an ultrafast FWM response, which in the case of a bare gold tip decays within few fs and can be effectively instantaneous in a non-resonant case [81]. The efficient 3rd-order nonlinear response of nanofocused SPPs has been a subject of a more detailed investigation, which revealed the existence of an additional nonlinearity mechanism enabled by high longitudinal field gradients associated with plasmon modes at the tip apex [149].

FWM signals generated at the tip apex are highly sensitive to the local field enhancement and can be used to probe local field distribution and corresponding fs-scale dynamics in a wide range of samples. Figure 5f shows the results of femtosecond near-field imaging of local plasmon dynamics in a thermally evaporated 100 nm thick gold film sample [81], where the gold tip is raster scanned at a few-nm distance above sample surface while the grating is illuminated with pairs of ~10 fs laser pulses producing nanofocused FWM at the tip apex. Upon scanning over the gold film edge, nanoscale regions with strong FWM signal (hot spots $S_{1,2,3}$) appear due to nonlinear polarization enhancement by localized surface plasmon resonances (LSPRs). These hot spots show different FWM decay dynamics, as observed in Fig. 5f where FWM images at different interpulse delays are normalized to the amplitude at region S_1. Fitting the experimental data with a model accounting for a Lorentzian response with resonant frequency ω_{res} and dephasing time T_2 yields similar resonance frequencies (800 nm and 790 nm) yet significantly different dephasing times T_2 (16 fs and 10 fs) as shown in Fig. 5g. These results manifest the first nonlinear optical spatio-temporal nano-imaging of coherent dynamics and demonstrate the potential of nanofocused FWM spectroscopy for investigating optical properties in a wide range of materials on nm-fs scales.

Nanofocusing-based nonlinear nano-imaging is particularly suitable for investigation of novel van der Waals 2D materials, where nanoscale inhomogeneities, grain boundaries, edges, and defects can crucially affect the local electron dynamics and associated optical properties. This has been demonstrated in the application of nanofocusing-based spectroscopy to study ultrafast coherent dynamics in graphene [82], with the

experimental configuration illustrated in Fig. 5h. The FWM signal is generated in graphene itself with in-plane polarization, and, despite the interaction area of only about 1000 carbon atoms, dominates over the FWM signal generated in the gold volume at the tip apex with out-of-plane polarization as shown in Fig. 5i. This strong graphene-generated FWM allows imaging its nanoscale distribution in the two-pulse excitation scheme with variable interpulse delay. Interestingly, the FWM intensity is enhanced at the edges as shown in Fig. 5j, with the spatial extent of the enhancement ranging from 100 to 400 nm scale, which exceeds the near-field localization by an order of magnitude. This delocalization behavior is attributed to Doppler broadening, which, due to the unusually high Fermi velocity in graphene v_F, limits the spatial resolution to scales of $\Delta L \simeq 2\pi v_F/\Delta\omega$, where $\Delta\omega$ is the bandwidth of the FWM response. From the results of time-resolved FWM nano-imaging shown in Fig. 5k and the modelling of FWM autocorrelation traces shown in Fig. 5l, a dephasing time T_2 in the range of 5 to 6 fs is obtained, which exhibits no discernible variation across the graphene flake and on the edges [82]. Such fast dephasing is attributed to efficient carrier-carrier scattering, which is screened only weakly in a 2D graphene sheet, and associated impact ionization as well as Auger recombination processes leading to rapid energy and momentum redistribution.

In contrast to the broadband response of graphene, the generation of nonlinear optical signals in 2D van der Waals semiconductors is strongly affected by the presence of excitonic resonances [80, 150, 151]. In monolayer transition metal dichalcogenide WSe_2 [80], the nonlinear optical response induced by nanofocused SPPs is complex and includes SHG due to the intrinsically broken inversion symmetry, 2-photon PL due to the A-exciton resonance, and FWM signal, which is extracted by fitting the measured spectrum and subtracting its SHG and 2-photon PL parts (Fig. 5d). Measurements of the local FWM autocorrelation traces in 1L WSe_2 with two-pulse nanofocused SPPs excitation under the tip apex and nano-imaging reveal a resonant response with dephasing times ranging from 5 to 60 fs with spatial variation on the 50 to 100 nm scale. This fast and spatially heterogeneous dephasing is attributed to thermally activated exciton-phonon interaction and disorder-induced scattering, which depends sensitively on the local presence of grain boundaries, line defects, and strain.

In addition to probing local femtosecond dynamics via FWM, the efficient third-order nonlinear optical response induced by nanofocused SPPs can be used to access vibrational resonances via CARS. It was shown that spectral focusing via ultrafast pulse shaping in combination with SPP nanofocusing on a gold tip achieves selective CARS excitation of a single Raman mode of carbon nanotubes [135], with corresponding spatial mapping on the nanoscale. The approach was further developed to demonstrate a new modality of CARS microscopy with simultaneous nanofocusing of phase-shaped 800 nm pump and 440 nm probe pulses on an aluminum tip [83]. Using this nanofocusing-based 2ω-CARS, an enhanced Raman response of the G- and 2D-bands in monolayer graphene was observed, and multi-walled carbon nanotubes were imaged using the D-, G-, and 2D-bands with spatial resolution of less than 90 nm (Fig. 5m).

3.2 Nanofocusing-based ultrafast electron microscopy

Beyond nonlinear optical nano-spectroscopy, plasmonic nanofocusing provides a promising approach towards new modalities of ultrafast electron microscopy. Photoemission from sharp metal tips under direct apex illumination with ultrashort laser pulses potentially allows for the development of point-like sources of high-brightness coherent femtosecond electron wavepackets for femtosecond point-projection microscopy (fsPPM) [152–155]. However, the spatial and temporal resolution achievable in fsPPM is ultimately limited by the tip-sample distance, which cannot be made much smaller than 10 μm due to undesired sample illumination. Plasmonic nanofocusing, with its efficient background-free confinement of optical field in the nanoscopic volume at the tip apex, allows for reducing the tip-sample distance down to sub-micrometer level and thus offers a powerful approach to improving the resolution of the fsPPM technique. Nanofocusing-based sources of ultrafast electron wavepackets have been experimentally demonstrated and studied in several works [145, 146, 156], with a typical setup shown in Fig. 6a. Inside an ultrahigh-vacuum (UHV) chamber, a few-cycle SPP pulse is launched on the tip shaft via grating coupling and propagates to the apex, undergoing adiabatic 3D compression of the optical mode. Electrons are generated at the apex in a multiphoton photoemission process, accelerated, and imaged with a microchannel plate (MCP) detector, a fluorescent screen, and a CMOS camera. From interferometric autocorrelation measurements shown in Fig. 6b, the electron pulse duration at the tip apex is extracted as 7.7 fs, which is only slightly longer than the original optical pump pulse duration of 5 fs [146] and enables the possibility for ultrafast electron microscopy with sub-10 fs temporal resolution. The nanofocusing-based electron point source has been used to image a single InP nanowire containing n- and p-doped segments [146], as shown in Fig. 6c. Here, the trajectories of tip-emitted electrons sensitively depend on local electric near fields in the vicinity of the nanowire [153], with the dominant deflection occurring in the nanowire-normal direction. Depending on the

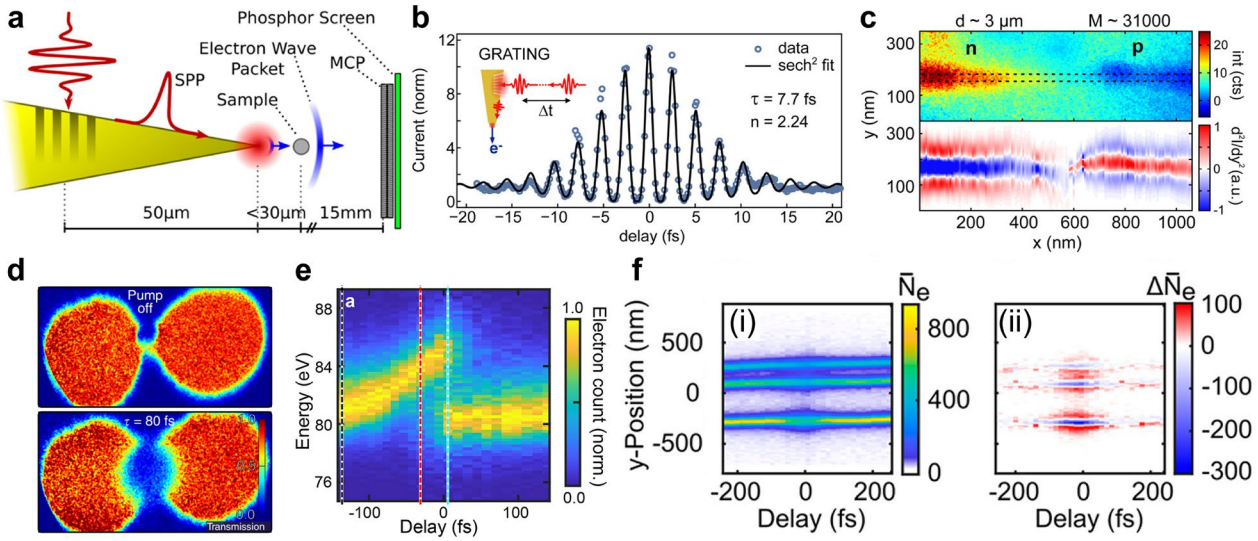

Fig. 6 Nanofocusing-based ultrafast point projection electron microscopy. **a** Schematic of the setup for remotely driven electron emission, with SPP wavepackets nanofocusing at the apex of a gold tip, which results in electron emission. Electrons are then detected in a point-projection setup. **b** Interferometric autocorrelation of the photoelectron current emitted from tip apex under grating-coupled nanofocused SPP excitation (circles) together with fit (curve) assuming sech^2 pulse shape. **c** Background-subtracted PPM image of the transition region of an individual InP nanowire in the nanofocused SPP-driven mode. **d** Point-projection image of a double-nanohole gold antenna recorded in the absence of a pump laser with nanofocused SPP-driven electron source. **e** Kinetic energy spectrum of photoelectrons emitted from a nanofocused SPP-driven tip and transmitted through the center of a double-nanohole gold antenna in UPEM as a function of pump-probe delay. **f** (i) Spatially and temporally resolved images of a Yagi-Uda slit antenna integrated along the slit axis measured in a nanofocusing-based UPEM. (ii) Corresponding differential images obtained by subtracting data in the absence of pump pulses

sign of the electric near fields, electrons are deflected either towards or away from the nanowire (black dashed lines), which translates into the opposite contrast for n- and p-doped regions seen in the resulting background-subtracted electron distribution (top panel) and in the second derivative of the corresponding Gaussian-fitted profiles (bottom panel), demonstrating spatial resolution on the order of tens of nanometers.

Further, the nanofocusing-based electron source has been used to implement UPEM with temporal resolution down to 25 fs [157]. Here, in a pump-probe experiment, electron wavepackets were generated via probe pulses at 1.8 µm wavelength nanofocused on a sharp gold tip, while a sample consisting of a nanogap antenna fabricated in a 30 nm thick gold film was excited by pump pulses derived from the same laser. Nanofocusing-generated electrons were accelerated towards the sample placed 2.7 µm away from the tip apex, diffracted by the sample, and captured by a distant MCP detector to obtain a 2D image as shown in Fig. 6d (top panel), with the two circles corresponding to the two nanoholes in the gold film where probe electrons are mostly transmitted without scattering. When the sample was optically pumped (bottom panel), a cloud of photoemitted electrons was generated in the nanogap, which resulted in the local reduction in probe electron transmission. By measuring the image on the detector as a function of the pump-probe time delay, the release and expansion dynamics of the pump-generated electron cloud photoemitted from the nanogap sample were captured with simultaneous spatiotemporal resolution of 20 nm and 25 fs, made possible by the reduced tip-sample distance in the nanofocusing configuration. The nanofocusing-based UPEM was developed further to incorporate a time-of-flight detector and additionally probe electron kinetic energy distribution shown in Fig. 6e, which allowed distinguishing between angular deflection of the probe electrons due to the transverse local field components and acceleration/deceleration due to the longitudinal local field components [158]. Recently, it was demonstrated that nanofocusing-based UPEM can be applied to directly probe optical near fields and corresponding ultrafast dynamics of a nanoscale Yagi-Uda antenna consisting of three parallel slots in a 13 nm thick gold film [159], with a characteristic spatiotemporal electron image shown in Fig. 6f-(i). The result of subtracting a reference signal obtained without optical pump reveals deflection of the probe electrons by transient near fields from regions inside the slots (blue, lower signal) to regions outside the slots (red, higher signal), with 80 fs dynamics defined by the antenna plasmon resonance as compared to 20 fs full width at half maximum of the pump pulses (Fig. 6f-(ii)).

4 Ultrafast STM

Exploring light-matter interactions at ultrafast timescales down to the femtosecond range and high spatial resolutions reaching the sub-ångström level has been a long-standing objective of scanning probe techniques. In recent years, related techniques have experienced significant progress with the emergence of ultrafast STM. The operation of ultrafast STM requires precise, high-speed control of quantum tunneling between the tip and sample. By applying ultrafast electromagnetic pulses to modulate the local electric field at the STM junction (Fig. 1a), rapid changes in the electron tunneling processes occur in response to the pulses, leading to the generation of a corresponding ultrafast current component. This enables ultrafast STM to achieve signal modulation for probing tunneling dynamics, providing temporal resolution down to the femtosecond scale as determined by the pulse duration. This cutting-edge technique combines the ability to resolve electronic density distribution down to the sub-ångström scale of STM with transient electromagnetic field control of the tunneling processes [160–162]. The light-assisted tunneling processes in the STM junction can be categorized into photon-driven tunneling and field-driven tunneling characterized by the Keldysh parameter γ ($\gamma = \sqrt{E_{barrier}/2U_P}$, where $E_{barrier}$ is tunneling barrier and U_P is ponderomotive kinetic energy) [163, 164] (Fig. 7a). Photon-driven tunneling dominates the tunneling process when $\gamma > 1$, as multiphoton absorption can excite electrons near the Fermi level in tunnel junction, thereby inducing electron tunneling. In contrast, when the local electric field in tunnel junction is sufficiently high ($\gamma < 1$), the potential barrier experiences a significant bend. Electrons can easily tunnel to the other side without the need for multiphoton absorption, facilitating a transition from photon-driven tunneling to field-driven tunneling. Recognizing these distinct tunneling mechanisms is crucial for elucidating the fundamental processes involved.

Despite achieving such high spatial resolution, introducing optical pulses into STM presents notable challenges, particularly the signal distortion due to thermal expansion [165] with incident photon energy at the visible light range or even higher frequencies. Recent studies have shown that light-induced thermal expansion can be significantly suppressed via either involving light of lower frequencies, extending down to the terahertz range, or by employing ultrashort laser pulses of durations even shorter than 6 fs [164, 166], due to their minimal thermal effects. Building on these developments, we review the critical influence of the carrier-envelope phase (CEP) in ultrashort pulses for ultrafast STM, introducing an ultrafast asymmetric electric field into the tunnel junction. This asymmetry significantly affects the tunneling dynamics within the STM junction, facilitating a more profound exploration of quantum states and the precise, coherent control over electronic and vibrational dynamics [162, 164, 167, 168].

An alternative strategy to mitigating thermal expansion is to extract the modulated ultrafast tunnel current by adopting delay-time modulation rather than laser intensity modulation [169–171]. In this approach, the tunnel current resulting from thermal expansion is filtered out as an averaged background, which will be discussed in detail in the "Lightwave-driven delay-time modulation STM" section. Consequently, the ultrafast components within the tunnel current can be isolated through the lock-in technique, enhancing the precision of ultrafast response. As a result of recent technological advancements, ultrafast STM has facilitated a plethora of unprecedented in-depth investigations into the electronic and vibrational dynamics in metals, semiconductors, molecules, 2D materials, and diverse quantum materials down to picometer spatial and femtosecond temporal resolution [160, 172–176].

4.1 Terahertz scanning tunneling microscopy

Recent advancements in THz techniques and the design of lightwave-driven STM have facilitated the integration of few-cycle THz pulses into STM, leading to the development of terahertz scanning tunneling microscopy (THz-STM). Traditional STM employs electronic approach to control the bias voltage applied to the STM tip for manipulating the tunneling process. Similarly, THz-STM relies on modulating the bias voltage, but this modulation is facilitated by THz pulses. This optical approach enables high-speed control, allowing THz-STM to achieve femtosecond temporal resolution. The key advantage of the application of THz pulses lies in the strong electric field and low photon energy, which leads to minimal absorption by a metallic tip and consequently negligible thermal effects [166]. This advantage allows researchers to perform ultrafast experiments in THz-STM alongside the conventional optical pump-probe techniques, effectively bypassing the issue of noise from thermal expansion.

Figure 7b outlines the schematic diagram of an early example of the experimental configuration of THz-STM [166]. Free-space terahertz pulses with a frequency range from 0.1 to 10 THz are focused on the STM tip, leading to a strong transient electric field confined at the tip apex. The oscillating electric field induces a voltage pulse in the STM junction, generating tunnel current. To extract the tunnel current induced by THz pulses, the system employs an optical chopper to modulate the intensity of THz pulses and a lock-in amplifier to demodulate the tunnel current signal. The principle of THz-STM is

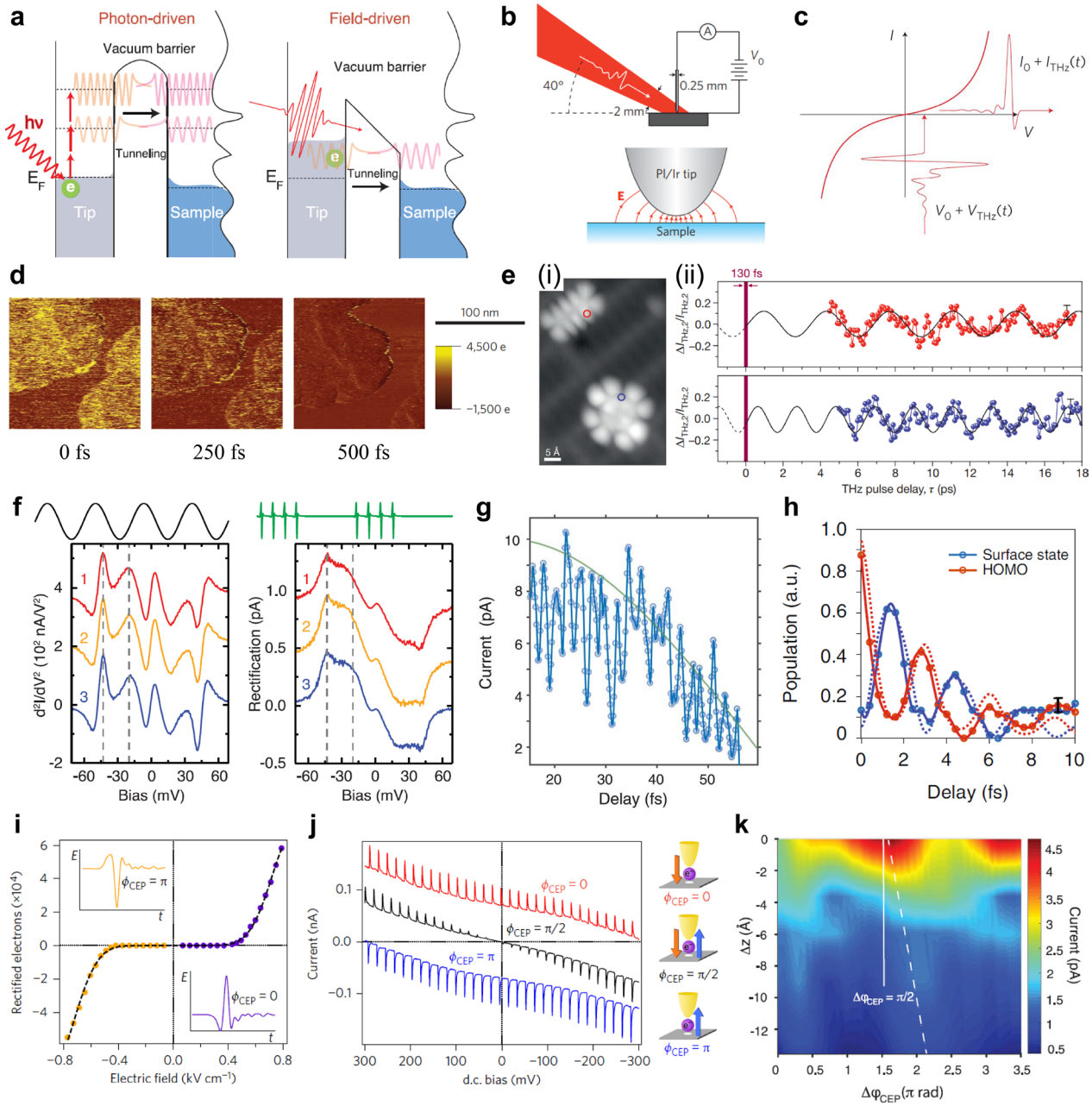

Fig. 7 Spatio-spectral-temporally resolved dynamics demonstrated by ultrafast STM and coherent manipulation of tunneling processes. **a** Illustration of the photon-driven tunneling process (left panel) and the field-driven tunneling process (right panel) in STM junction. **b** Schematic of a terahertz scanning tunneling microscope (top panel) and electric field enhancement at the apex of tip (bottom panel). **c** Nonlinear relationship between the tunnel current and the voltage across the tunnel junction. The application of bias voltage results in an asymmetric tunnel current response with a significant rectified component. **d** THz-STM autocorrelation images of gold islands on HOPG from 0 fs to 500 fs, in intervals of 250 fs. **e** (i) Constant-current STM image of a pentacene molecule HOMO (top left) and a copper phthalocyanine molecule HOMO (bottom right). (ii) THz-STM measurements performed on these different molecules, with positions marked with the red and blue circles shown in the left panel, indicating distinct coherent molecular oscillations. **f** IETS (left panel) and TRS (right panel) measurements of H_2 molecule at three positions on a Cu_2N island. **g** Tunnel current measured on a gold nanorod, revealing temporal oscillations of LSPRs. **h** Electron population evolution of coherent interference between the HOMO and surface state. **i** Count of rectified electrons induced by incident electric fields at different CEPs ($\phi = 0, \pi$). **j** Rectified current variation with bias voltage at three different CEPs ($\phi = 0, \pi/2, \pi$). The right panel shows distinct electron motion behaviors corresponding to the CEPs. **k** Tunnel current as a function of CEPs with different tunnel gap widths. The bias voltage is 100 mV. The white dashed line represents the maximum values of the tunnel current for varying the tunnel gaps

based on the I–V dependence of the tunnel junction (Fig. 7c), which is depicted by the Simmons model [166]. Considering the nonlinear I–V dependence and that the measured tunnel current results from integrating the lightwave-driven current over time, applying a bias voltage to the STM tip is crucial for obtaining a sufficient rectified component of the tunnel current, which arises from the asymmetric response. In the early example shown in Fig. 7d, THz-STM autocorrelation measurements investigating carrier dynamics were performed with gold islands deposited on a highly ordered pyrolytic graphite (HOPG) substrate, demonstrating 2 nm spatial and subpicosecond (< 500 fs) temporal resolution at room temperature. In subsequent studies [160, 161, 172, 173], the integration of THz-STM with low-temperature facilitated higher spatial resolution, reaching ångström scale at around 100 K, and sub-ångström precision at temperatures near 10 K. With this superior spatiotemporal resolution, THz-STM enables direct observation of quantum coherence [162], the distribution of local density of states (LDOS) [176, 177], charge density waves [178], and provides access to phase-resolved spectroscopy [179] and luminescence spectroscopy [180].

In addition to probing electronic dynamics, THz-STM can unravel vibrational dynamics, e.g., the dynamics of pentacene molecules on a monolayer sodium chloride island that electrically insulates the molecules from the underlying gold substrate, forming a classical double-barrier geometry [160]. With the strong electric field of THz pulses, the Fermi level of the tip can be aligned with the substrate and molecular orbitals, such as the lowest unoccupied molecular orbital (LUMO) or the highest occupied molecular orbital (HOMO), enabling electron tunneling. During the tunneling process, an electron tunnels from the molecular orbital to the tip, resulting in the molecule being temporarily charged, which triggers oscillations of the molecule in the tunnel junction as a result of altered Coulomb and van der Waals interactions. This allowed the observation of coherent oscillations in tunnel current, originating from the distinct motion of pentacene and copper phthalocyanine molecules (Fig. 7e). The measured current oscillations at marked positions on the constant-current STM image exhibit different frequencies (Red: 0.3 THz. Blue: 0.5 THz), correlating with molecular properties. Further, the atomic-scale force pulse originating from breaking the equilibrium of force can induce ultrafast switching in molecular structural configurations. For instance, the ultrafast force generated by THz-STM can be utilized to switch a magnesium phthalocyanine (MgPc) molecule between two stable adsorption geometries within a double-well potential [174]. Overall, by investigating molecular motion dynamics through current oscillations, THz-STM showcases the capability to probe ultrafast processes at the molecular level.

To enhance functionality further, molecules in tunnel junctions of THz-STM are frequently employed as ultrafast switches and coherent sensors. Based on the previous work [174], the MgPc molecule has been demonstrated to function as an ultrafast switch by altering its adsorption geometries on the substrate in response to a transient THz electric field [181]. Moreover, the switching rate of the MgPc molecule between two stable adsorption geometries is discovered to have a strong correlation with the voltage waveform inside the STM junction, making the molecule an effective atomic-scale voltage gauge. Utilizing these properties, reconstruction of the transient near field confined around the STM junction is successfully realized. These works have inspired further research [182] on the non-destructive methods for probing the near-field waveform within the STM junction. By integrating THz-STM with THz pulse cross-correlations, spectral measurements of THz near field in the tunnel junction have been successfully demonstrated, eliminating the requirement for molecules to serve as ultrafast switches. Moreover, H_2 molecule was demonstrated to serve as a quantum sensor for imaging the surface heterogeneity of Cu_2N islands on a Cu(100) surface [161]. When the energy of tunneling electrons was sufficient to excite vibrational or rotational states of the H_2 molecule, the THz pulse drove a coherent oscillation of the H_2 molecule, resulting in a significant change in the population of two distinct adsorption configurations of the molecule. Utilizing the coherent oscillations of the molecular two-level system, which exhibits extreme sensitivity to the applied electric field [183] and the underlying atomic composition of the Cu_2N/Cu(100) system, an enhancement in spatial resolution can be achieved. Conventional inelastic electron tunneling spectroscopy (IETS) was performed to confirm the presence of the H_2 molecule, and a comparison with IETS results indicated that terahertz rectification spectroscopy (TRS) also effectively drives excitation processes (Fig. 7f). Further conducting THz-STM measurements in TRS mode can result in improved signal contrast relative to both IETS and single beam TRS, enabling sub-ångström spatial resolution and femtosecond temporal resolution with energy-level resolution in the GHz range.

4.2 Ultrashort near-infrared pulse scanning tunneling microscopy

As the pulse duration becomes ultrashort, the coupling between laser pulse and atomic lattice diminishes even at NIR frequencies, resulting in a notable suppression of thermal effects. Considering that the employed ultrashort pulses are typically few-cycle in nature, their

characteristics are profoundly influenced by the pulse's CEP, which makes the utilization of CEP-stable pulses essential. For example, by employing CEP-stable ultrashort (< 6 fs) NIR (~810 nm) pulses, the manipulation of electrons by varying tunnel gaps, bias voltages, and CEPs of pulses was investigated in the field-driven regime [164]. Using this precise setup, the coherent relaxation dynamics of LSPRs with ~40 fs characteristic time in a gold nanorod can be observed (Fig. 7g). In the subsequent study shown in Fig. 7h, the quantum coherent interference excited in perylenetetracarboxylic dianhydride (PTCDA) molecules by orthogonally polarized pulses was explored in the photon-driven regime [162]. By changing the delay time between the orthogonally polarized CEP-stable ultrashort pulses, the polarization of the total electric field can be manipulated to investigate coherent interference among the HOMO, LUMO, and surface state of Au(111).

4.3 Coherent manipulation in ultrafast STM

Coherence is an important and fascinating characteristic of ultrafast laser pulses. As to the tunneling processes assisted by the ultrafast laser, the phase information from the ultrafast laser is coherently transferred to the samples within the tunnel junction, including but not limited to atoms, molecules, and semiconductors. This opens up new opportunities to investigate the quantum coherent phenomena and their dynamics inside the tunnel junctions. Moreover, the phase of the ultrafast pulse gains further significance when the ultrafast laser pulse (including both THz laser pulse and ultrashort laser pulses) approaches the few cycles or even half-cycle limit. Under such conditions, the CEP of the ultrashort pulse becomes critical, influencing the electric field's polarity and subsequently controlling the tunneling process.

Precisely controlling the CEPs of laser pulses is important for achieving ultrafast coherent manipulation of tunnel electrons. Recently, the manipulation of tunnel electrons in the STM junction by controlling the CEP of a single-cycle THz pulse was achieved [167, 168]. When no bias voltage is applied to the tunnel junction, the rectified electrons exhibit opposite responses corresponding to the CEP of THz pulse at 0 and π (Fig. 7i). The dashed line calculated using the Simmons model, aligns closely with the experimental results. Figure 7j shows the tunnel current in relation to the bias voltage for three distinct CEPs: 0, $\pi/2$, and π, while the right panels depict the corresponding motions of tunnel electrons at these respective CEPs. The remarkable feature observed in these curves is the occurrence of pulse trains as the bias voltage changes, which is evidence that the current is generated in a tunnel junction, proving the coherent manipulation capabilities of both the bias voltage and the CEP. Figure 7k also indicates the influence of the tunnel gap on the tunnel current [164]. It was shown that a decrease in the tunnel gap by 1 nm can lead to a reduction of approximately 600 as in the time required for electrons to tunnel through the barrier. These findings are motivating for the future advancement of coherently manipulating tunneling processes on a sub-femtosecond timescale.

4.4 Lightwave-driven delay-time modulation STM

In addition to the efforts to mitigate thermal expansion by employing THz and ultrashort pulses, researchers have demonstrated an alternative approach to isolate noise originating from thermal expansion. Unlike the previously mentioned techniques which modulate pulse intensity, the key idea of this strategy is to modulate the delay time between pump and probe pulses instead (Fig. 8a), leaving the thermal expansion of the tunnel junction as an averaged background to a large extent [184]. Consequently, the tunnel current originating from the thermal expansion exhibits a different frequency compared to the current from optically excited phenomena, which effectively suppresses signal interference from thermal effects through lock-in demodulation. The delay-time modulation techniques, which are mainly discrete modulation methods, can be implemented using pulse pickers [169] and switching optical paths [185], among other techniques [186]. These discrete modulation approaches not only further suppress noise but also broaden the scanning range of the delay time. Therefore, the delay-time modulation STM has been demonstrated as a versatile technique in visible light and NIR range, capable of measuring an extensive array of characteristic times. This versatility enables it to explore various phenomena, including photoinduced carrier dynamics [169, 186], spin dynamics [187] and many-body dynamics [185], among others, showcasing its broad applicability in uncovering intricate dynamic processes.

Compared with the conventional pump-probe technique, delay-time modulation STM offers a distinctive capability to study physical phenomena with remarkably long relaxation times, extending into the microsecond scale. Figure 8b shows the heterogeneous charge dynamics on the n-type GaAs(110) substrate, highlighting individual ionized donors beneath the surface [170]. These ionized donors can capture photocarriers generated by laser pulses, thereby reverting to neutral donors and leading to heterogeneity in the decay times in their vicinity. This study revealed that the decay constant is connected to the donor binding energy and the local electric field, and it also examined the variation of the binding energy with the distance to the surface. In another implementation, the relaxation dynamics of polarons bound to oxygen vacancies on the surface of rutile TiO_2(110) was

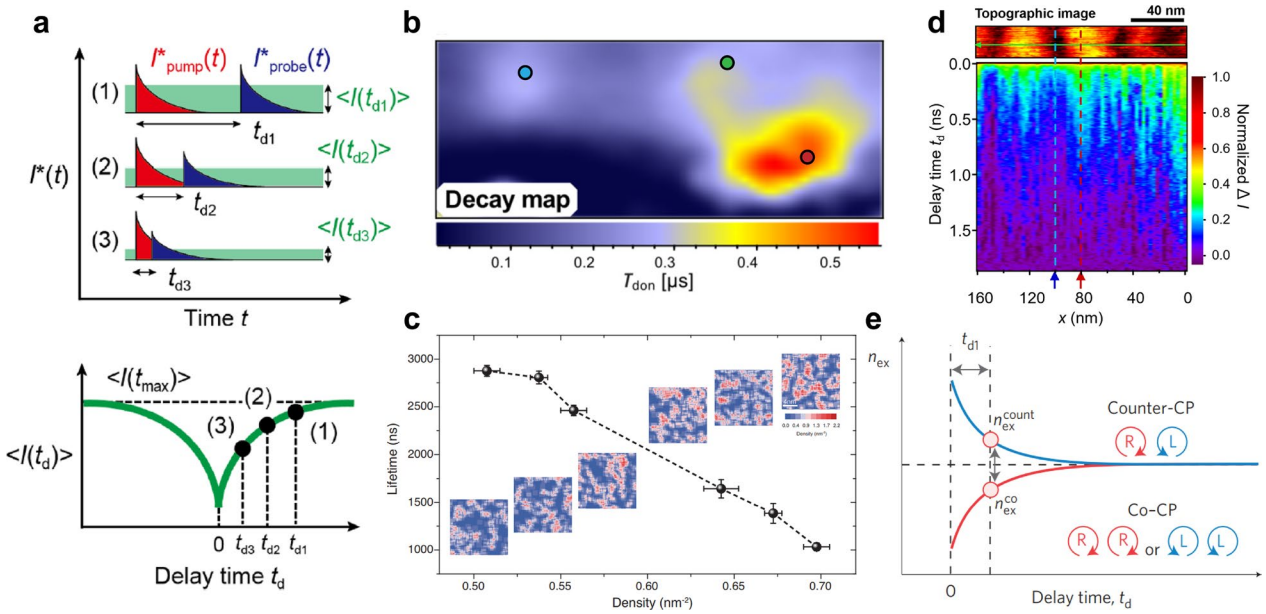

Fig. 8 Ultrafast delay-time modulation STM. **a** Principle of tunnel current signal extraction through delay-time modulation. **b** Decay time mapping on the n-type GaAs(110) surface with donors beneath the surface (three donors shown as colored dots: red for nearest, blue for farthest to the surface). **c** Lifetimes of free electrons versus defect density, with its distributions shown in the insets. **d** STM image on the WS_2 ripple (top panel) and corresponding ultrafast STM measurement performed (bottom panel). The blue and red dashed lines indicate the bottom and top of the ripple, respectively. **e** Spin detection signal versus delay time with different mixing degree of circular polarizations of pump and probe pulses: counter-CP and co-CP

investigated [171]. Lattice defects in TiO_2 can scatter the electrons, resulting in changes to their lifetimes and energy states. Figure 8c depicts how the lifetime of free electrons in the conduction band changes with defect density. It is noteworthy that the lifetime is minimally influenced by the spatial distribution of defects, as shown in the insets. Recently, exciton dynamics associated with many-body effects in a WS_2 ripple, such as exciton-exciton annihilation (EEA), has been investigated by delay-time modulation STM as well (Fig. 8d). The variation in EEA dynamics between the top and bottom of the ripple arises from the interaction between the ripple structure and the substrate, influencing the excitonic behavior and thus altering the observed tunnel current. As the tunnel current is positively correlated with exciton dissociation and exciton density, and the probability of exciton dissociation is also associated with exciton density, observing the variation in the normalized ΔI allows for analyzing the EEA dynamics in the region beneath the tip [185].

Improvements to the instrumental configuration to expand the functionality of delay-time modulation STM are ongoing. In the study depicted in Fig. 8d, two contact mode AFM tips serving as drain and source electrodes of monolayer WS_2/WSe_2 in-plane heterostructure were incorporated into the system [185]. Thus, current flow can be continuously monitored while conducting measurements, enabling the distinction of high-resistive grain boundaries in WS_2. This allows for the examination of the dynamic processes depending on grain sizes. To explore a broader range of physical phenomena, the optical pump-probe technique utilized in delay-time modulation can also be refined. Figure 8e shows the further developed circular polarization modulation STM, which was demonstrated to observe the spin dynamics at the nanoscale [187]. As electron spins can be optically oriented by circularly polarized laser pulses, the spin relaxation following excitation by these pulses can be monitored, thereby enabling the investigation of important physical phenomena such as quantum beats of spin precession. The consistent and inconsistent circular polarizations of pump and probe pulses are referred to as co-circularly polarized (co-CP) and counter-circularly polarized (counter-CP), respectively. The signal difference between these two modes can be acquired through delay-time modulation, facilitating the investigation of spin dynamics with atomic-scale spatial resolution and subpicosecond temporal resolution.

5 Summary and outlook

This review explores the underlying principles and associated applications of three distinct ultrafast microscopy techniques. Additionally, we present a

three-dimensional depiction of ultrafast tip-based microscopy (Fig. 9), demonstrating that both spatial resolution at the sub-ångström scale and temporal resolution at the femtosecond scale have been achieved, with probe frequency effectively spanning the NIR to far-infrared (FIR) spectrum.

Through the three-dimensional representation, a comprehensive comparative analysis of the three techniques can be conducted. Ultrafast STM provides the highest spatial resolution among tip-based microscopy techniques, while its temporal resolution awaits further improvement. Moreover, the practical application of this technique is often constrained by the requirements for cryogenic environments and UHV conditions. In contrast, ultrafast nanofocusing offers exceptional temporal resolution down to a few femtoseconds due to coherent excitation in the nonlinear optical regime [188]; yet, enhancing its spatial resolution remains a challenge, with the probe frequency range also being notably restricted. Both of the above two techniques currently lack studies in the MIR range, while *s*-SNOM has been extensively demonstrated in this spectral band. However, the spatiotemporal resolution of *s*-SNOM requires further improvement.

The above analysis shows that although these three techniques have covered a wide range of probe frequencies and are actively pursuing higher spatiotemporal resolution as well as broader spectral coverage, there are many aspects yet to be investigated. From the three-dimensional representation, it is evident that probe frequency in the visible and higher frequency ranges, as well as attosecond-scale dynamics, are largely unexplored. In terms of broadening frequency coverage, ultrafast *s*-SNOM is in principle compatible with diverse frequencies, and recent advancements in ultrafast nanofocusing with broadband spectral sources [144] and THz sources [189] are also expected to further expand the probe frequency range. At the same time, achieving attosecond-scale temporal resolution in the field of ultrafast near-field optical microscopy is highly desirable, as it would allow for the direct study of electron motion and other rich physical phenomena.

In addition, some advanced techniques have been developed with the potential to enhance ultrafast tip-based microscopy. For example, research on THz *s*-SNOM has recently increased due to its low-energy excitation [106, 190–193]. More extensive studies of THz *s*-SNOM are expected to lead to future developments of

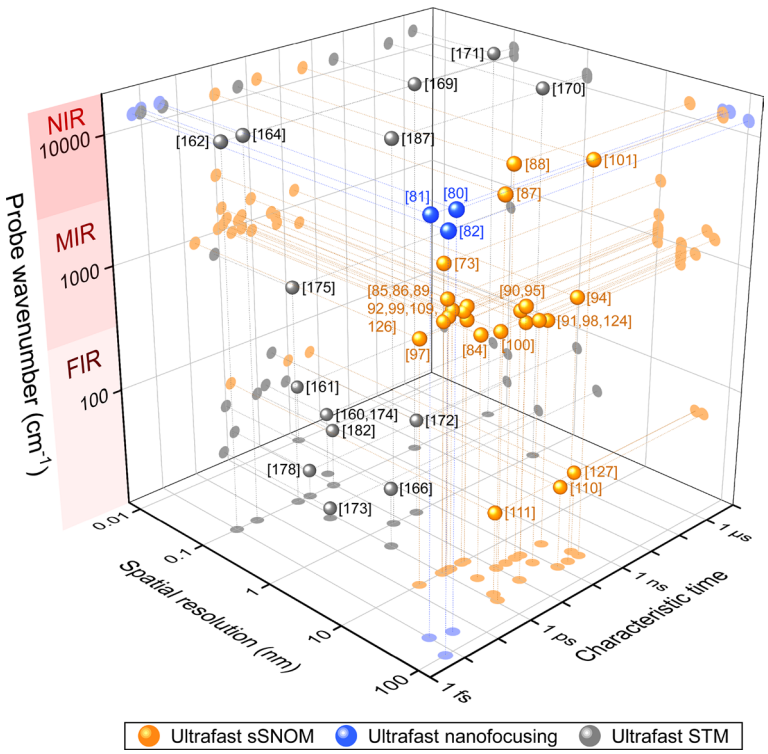

Fig. 9 Three-dimensional representation of spatio-spectral-temporal measurement parameters. This plot aggregates experimental data points from the literature, showcasing the spatial resolution, characteristic time, and probe wavenumber of each data point. Each data point corresponds to reported values from a specific study, illustrating the current state-of-the-art capabilities in ultrafast near-field microscopy. Axes represent spatial resolution, characteristic time, and probe wavenumber, respectively

ultrafast THz *s*-SNOM. Notably, the integration of cryogenic techniques into ultrafast *s*-SNOM experiments has not yet been developed, but the potential benefits are substantial. This approach will facilitate the study of more novel physical phenomena that cannot be observed at room temperature, such as high-mobility graphene and long-lived polaritons. However, the combination of cryogenic techniques presents technical challenges, such as the need for a cryogenic scanner with a long travel range, while the operation of ultrafast *s*-SNOM at low temperatures also faces difficulties. Moreover, artificial intelligence algorithms and machine learning techniques, including compressed sensing [194] and hybrid neural networks [195], have been integrated into data processing for nano-spectroscopy and nano-imaging, demonstrating the ability to improve acquisition efficiency and sensitivity. Additionally, new techniques are emerging in the field of ultrafast tip-based microscopy. Near-field optical tunneling emission (NOTE) was recently demonstrated as a new type of ultrafast SPM [196], enabling access to atomic-scale spatial resolution and allowing observation of the tunnel current within a subcycle. Compared to conventional lightwave-driven STM, NOTE is not limited to conductive materials and can measure insulating materials.

The future applications of ultrafast techniques can significantly broaden the exploration of more diverse material systems, such as the investigation of Rabi oscillations in a single emitter, topological insulators that provide insight into edge-state dynamics, and emerging material platforms like 2D moiré superlattice known for their correlated electronic phases. These systems offer exciting opportunities for exploring novel phenomena using ultrafast tip-based microscopy. Moreover, these ultrafast techniques have potential applications in the field of quantum technology. In quantum information science, defects and heterogeneities can lead to premature loss of quantum coherence. Nano-imaging can help identify these heterogeneities, while ultrafast implementations can reveal how defects induce electronic or phononic scattering associated with decoherence. Furthermore, exploring strong coupling in light-matter hybrid states remains relevant for quantum applications, suggesting that ultrafast nano-spectroscopy and nano-imaging techniques could enhance our understanding of the behaviors of these materials.

In conclusion, this review presents the significant advancements enabled by ultrafast tip-based microscopy in the exploration of nanoscale phenomena, offering remarkable spatiotemporal resolution. Three representative techniques in ultrafast tip-based microscopy, namely ultrafast *s*-SNOM, ultrafast nanofocusing and ultrafast STM, have greatly advanced the understanding of underlying physical mechanisms, enabling the direct observation of dynamic processes at the atomic scale. Continued progress in this field promises to further enhance the ability to investigate complex physical phenomena, driving both advanced scientific discovery and the development of cutting-edge techniques.

Acknowledgements
The authors thank Lei Zhou for his valuable discussion.

Author contributions
Z.Z. (Zhichen Zhao) and V.K. wrote the manuscript. T.J. supervised this work. All authors read and approved the final manuscript.

Funding
Z.Z. (Zhichen Zhao) and T.J. acknowledge the support from the National Natural Science Foundation of China (62175188, 62475194) and the Science and Technology Commission of Shanghai Municipality (23190712300, 23ZR1465800). X.C. acknowledges support from the National Natural Science Foundation of China (61925504). V.K. acknowledges support from the Priority 2030 Federal Academic Leadership Program. D.H. acknowledges the support from the National Natural Science Foundation of China (62305249). Z.W. (Zhanshan Wang) acknowledges support from the National Natural Science Foundation of China (62192770, 62192772). M.B.R. acknowledges support from the National Science Foundation (NSF) Science and Technology Center on Real-Time Functional Imaging (STROBE) under Grant DMR 1548924 for ultrafast pump-probe nano-imaging instrument development, the National Science Foundation (NSF GrantNo. CHE2108009) for strong light matter coupling, and the U.S. Department of Energy, Office of Basic Sciences, Division of Material Sciences and Engineering, under award no. DESC0008807 for coherent nano-imaging of quantum materials.

Availability of data and materials
Not applicable.

Declarations

Competing interests
The authors declare that they have no competing interests.

Received: 1 September 2024 Revised: 20 October 2024 Accepted: 5 November 2024
Published online: 13 January 2025

References

1. Q. Zhang et al., Interface nano-optics with van der Waals polaritons. Nature **597**, 187–195 (2021)
2. D. Basov, M. Fogler, F. García de Abajo, Polaritons in van der Waals materials. Science **354**, aag1992 (2016)
3. T. Low et al., Polaritons in layered two-dimensional materials. Nat. Mater. **16**, 182–194 (2017)
4. X. Guo et al., Polaritons in van der Waals heterostructures. Adv. Mater. **35**, 2201856 (2023)
5. G. Hu, J. Shen, C.-W. Qiu, A. Alù, S. Dai, Phonon polaritons and hyperbolic response in van der Waals materials. Adv. Opt. Mater. **8**, 1901393 (2020)
6. J.D. Caldwell et al., Low-loss, infrared and terahertz nanophotonics using surface phonon polaritons. Nanophotonics **4**, 44–68 (2015)
7. W. Ma et al., In-plane anisotropic and ultra-low-loss polaritons in a natural van der Waals crystal. Nature **562**, 557–562 (2018)
8. Z. Zheng et al., A mid-infrared biaxial hyperbolic van der Waals crystal. Sci. Adv. **5**, eaav8690 (2019)
9. Y. Wu et al., Manipulating polaritons at the extreme scale in van der Waals materials. Nat. Rev. Phys. **4**, 578–594 (2022)

10. C. In, U.J. Kim, H. Choi, Two-dimensional Dirac plasmon-polaritons in graphene, 3D topological insulator and hybrid systems. Light Sci. Appl. **11**, 313 (2022)
11. Y. Qu et al., Tunable planar focusing based on hyperbolic phonon polaritons in α-MoO_3. Adv. Mater. **34**, 2105590 (2022)
12. X. Guo et al., Hyperbolic whispering-gallery phonon polaritons in boron nitride nanotubes. Nat. Nanotechnol. **18**, 529–534 (2023)
13. G. Hu et al., Topological polaritons and photonic magic angles in twisted α-MoO_3 bilayers. Nature **582**, 209–213 (2020)
14. Q. Zhang et al., Hybridized hyperbolic surface phonon polaritons at α -MoO_3 and polar dielectric interfaces. Nano Lett. **21**, 3112–3119 (2021)
15. W. Ma et al., Ghost hyperbolic surface polaritons in bulk anisotropic crystals. Nature **596**, 362–366 (2021)
16. Q. Zhang et al., Unidirectionally excited phonon polaritons in high-symmetry orthorhombic crystals. Sci. Adv. **8**, eabn9774 (2022)
17. X. Guo et al., Mid-infrared analogue polaritonic reversed Cherenkov radiation in natural anisotropic crystals. Nat. Commun. **14**, 2532 (2023)
18. G. Hu et al., Real-space nanoimaging of hyperbolic shear polaritons in a monoclinic crystal. Nat. Nanotechnol. **18**, 64–70 (2023)
19. H. Lee et al., All-optical control of high-purity trions in nanoscale waveguide. Nat. Commun. **14**, 1891 (2023)
20. D. Timmer et al., Plasmon mediated coherent population oscillations in molecular aggregates. Nat. Commun. **14**, 8035 (2023)
21. Z. Zhou et al., Gate-tuning hybrid polaritons in twisted α-MoO_3/graphene heterostructures. Nano Lett. **23**, 11252–11259 (2023)
22. S. Sunku et al., Photonic crystals for nano-light in moiré graphene superlattices. Science **362**, 1153–1156 (2018)
23. G. Hu, A. Krasnok, Y. Mazor, C.-W. Qiu, A. Alù, Moiré hyperbolic metasurfaces. Nano Lett. **20**, 3217–3224 (2020)
24. N.P. Wilson, W. Yao, J. Shan, X. Xu, Excitons and emergent quantum phenomena in stacked 2D semiconductors. Nature **599**, 383–392 (2021)
25. L. Du et al., Moiré photonics and optoelectronics. Science **379**, eadg0014 (2023)
26. Y. Jiang, S. Chen, W. Zheng, B. Zheng, A. Pan, Interlayer exciton formation, relaxation, and transport in TMD van der Waals heterostructures. Light Sci. Appl. **10**, 72 (2021)
27. Y. Xu et al., Correlated insulating states at fractional fillings of moiré superlattices. Nature **587**, 214–218 (2020)
28. Y. Cao et al., Correlated insulator behaviour at half-filling in magic-angle graphene superlattices. Nature **556**, 80–84 (2018)
29. Y. Cao et al., Unconventional superconductivity in magic-angle graphene superlattices. Nature **556**, 43–50 (2018)
30. K.L. Seyler et al., Signatures of moiré-trapped valley excitons in $MoSe_2$/WSe_2 heterobilayers. Nature **567**, 66–70 (2019)
31. C. Jin et al., Observation of moiré excitons in WSe_2/WS_2 heterostructure superlattices. Nature **567**, 76–80 (2019)
32. K. Tran et al., Evidence for moiré excitons in van der Waals heterostructures. Nature **567**, 71–75 (2019)
33. E.M. Alexeev et al., Resonantly hybridized excitons in moiré superlattices in van der Waals heterostructures. Nature **567**, 81–86 (2019)
34. G. Chen et al., Tunable correlated Chern insulator and ferromagnetism in a moiré superlattice. Nature **579**, 56–61 (2020)
35. Y. Jiang et al., Charge order and broken rotational symmetry in magic-angle twisted bilayer graphene. Nature **573**, 91–95 (2019)
36. R. Ribeiro-Palau et al., Twistable electronics with dynamically rotatable heterostructures. Science **361**, 690–693 (2018)
37. P. Roushan et al., Topological surface states protected from backscattering by chiral spin texture. Nature **460**, 1106–1109 (2009)
38. H. Beidenkopf et al., Spatial fluctuations of helical Dirac fermions on the surface of topological insulators. Nat. Phys. **7**, 939–943 (2011)
39. A. Soumyanarayanan, N. Reyren, A. Fert, C. Panagopoulos, Emergent phenomena induced by spin-orbit coupling at surfaces and interfaces. Nature **539**, 509–517 (2016)
40. Y. Xia et al., Observation of a large-gap topological-insulator class with a single Dirac cone on the surface. Nat. Phys. **5**, 398–402 (2009)
41. J.E. Moore, The birth of topological insulators. Nature **464**, 194–198 (2010)
42. D.J. Rizzo et al., Topological band engineering of graphene nanoribbons. Nature **560**, 204–208 (2018)
43. S. Guddala et al., Topological phonon-polariton funneling in midinfrared metasurfaces. Science **374**, 225–227 (2021)
44. M. Li et al., Topologically reconfigurable magnetic polaritons. Sci. Adv. **8**, eadd6660 (2022)
45. M. Wang et al., Spin-orbit-locked hyperbolic polariton vortices carrying reconfigurable topological charges. Elight **2**, 12 (2022)
46. L. Orsini et al., Deep subwavelength topological edge state in a hyperbolic medium. Nat. Nanotechnol. **19**, 1–6 (2024)
47. E. Abbe, Beiträge zur theorie des mikroskops und der mikroskopischen wahrnehmung. Archiv für mikroskopische Anatomie **9**, 413–468 (1873)
48. S.W. Hell, Far-field optical nanoscopy. Science **316**, 1153–1158 (2007)
49. G. Binnig, C.F. Quate, C. Gerber, Atomic force microscope. Phys. Rev. Lett. **56**, 930 (1986)
50. G. Binnig, H. Rohrer, C. Gerber, E. Weibel, Surface studies by scanning tunneling microscopy. Phys. Rev. Lett. **49**, 57 (1982)
51. G. Binnig, H. Rohrer, C. Gerber, E. Weibel, Tunneling through a controllable vacuum gap. Appl. Phys. Lett. **40**, 178–180 (1982)
52. E. Synge, Xxxviii. A suggested method for extending microscopic resolution into the ultra-microscopic region. London Edinburgh Dublin Philos. Mag. J. Sci. **6**, 356–362 (1928)
53. J.A. O'Keefe, Resolving power of visible light. JOSA **46**, 359 (1956)
54. E. Ash, G. Nicholls, Super-resolution aperture scanning microscope. Nature **237**, 510–512 (1972)
55. R.M. Stöckle, Y.D. Suh, V. Deckert, R. Zenobi, Nanoscale chemical analysis by tip-enhanced Raman spectroscopy. Chem. Phys. Lett. **318**, 131–136 (2000)
56. N. Hayazawa, Y. Inouye, Z. Sekkat, S. Kawata, Metallized tip amplification of near-field Raman scattering. Opt. Commun. **183**, 333–336 (2000)
57. Y. Koo et al., Dynamical control of nanoscale light-matter interactions in low-dimensional quantum materials. Light Sci. Appl. **13**, 30 (2024)
58. D.Y. Lee et al., Adaptive tip-enhanced nano-spectroscopy. Nat. Commun. **12**, 3465 (2021)
59. A.C. Gadelha et al., Localization of lattice dynamics in low-angle twisted bilayer graphene. Nature **590**, 405–409 (2021)
60. M. Kang et al., Conformational heterogeneity of molecules physisorbed on a gold surface at room temperature. Nat. Commun. **13**, 4133 (2022)
61. M. Brehm, T. Taubner, R. Hillenbrand, F. Keilmann, Infrared spectroscopic mapping of single nanoparticles and viruses at nanoscale resolution. Nano Lett. **6**, 1307–1310 (2006)
62. A. Dazzi, R. Prazeres, F. Glotin, J. Ortega, Local infrared microspectroscopy with subwavelength spatial resolution with an atomic force microscope tip used as a photothermal sensor. Opt. Lett. **30**, 2388–2390 (2005)
63. H. Wang, L. Wang, D.S. Jakob, X.G. Xu, Tomographic and multimodal scattering-type scanning near-field optical microscopy with peak force tapping mode. Nat. Commun. **9**, 2005 (2018)
64. Q. Xie, X.G. Xu, Fourier-transform atomic force microscope-based photothermal infrared spectroscopy with broadband source. Nano Lett. **22**, 9174–9180 (2022)
65. Q. Xie, Y. Zhang, E. Janzen, J.H. Edgar, X.G. Xu, Atomic-force-microscopy-based time-domain two-dimensional infrared nanospectroscopy. Nat. Nanotechnol. **19**, 1108–1115 (2024)
66. H.A. Bechtel, E.A. Muller, R.L. Olmon, M.C. Martin, M.B. Raschke, Ultrabroadband infrared nanospectroscopic imaging. Proc. Natl. Acad. Sci. **111**, 7191–7196 (2014)
67. O. Khatib, H.A. Bechtel, M.C. Martin, M.B. Raschke, G.L. Carr, Far infrared synchrotron near-field nanoimaging and nanospectroscopy. ACS Photonics **5**, 2773–2779 (2018)
68. I.D. Barcelos et al., Probing polaritons in 2D materials with synchrotron infrared nanospectroscopy. Adv. Opt. Mater. **8**, 1901091 (2020)
69. R. Hamers, D.G. Cahill, Ultrafast time resolution in scanned probe microscopies. Appl. Phys. Lett. **57**, 2031–2033 (1990)
70. R. Ulbricht, E. Hendry, J. Shan, T.F. Heinz, M. Bonn, Carrier dynamics in semiconductors studied with time-resolved terahertz spectroscopy. Rev. Mod. Phys. **83**, 543–586 (2011)
71. M. Tang, Y. Han, D. Jia, Q. Yang, J.-X. Cheng, Far-field super-resolution chemical microscopy. Light Sci. Appl. **12**, 137 (2023)
72. Z. Schumacher, A. Spielhofer, Y. Miyahara, P. Grutter, The limit of time resolution in frequency modulation atomic force microscopy by a pump-probe approach. Appl. Phys. Lett. **110**, 053111 (2017)
73. S.A. Donges et al., Ultrafast nanoimaging of the photoinduced phase transition dynamics in VO_2. Nano Lett. **16**, 3029–3035 (2016)

74. L. Novotny, B. Hecht, *Principles of Nano-optics* (Cambridge University Press, 2012)
75. G. Ni et al., Fundamental limits to graphene plasmonics. Nature **557**, 530–533 (2018)
76. G. Ni et al., Long-lived phonon polaritons in hyperbolic materials. Nano Lett. **21**, 5767–5773 (2021)
77. Y. Zhou et al., Thermal and electrostatic tuning of surface phonon-polaritons in $LaAlO_3/SrTiO_3$ heterostructures. Nat. Commun. **14**, 7686 (2023)
78. A. Anderson, K.S. Deryckx, X.G. Xu, G. Steinmeyer, M.B. Raschke, Few-femtosecond plasmon dephasing of a single metallic nanostructure from optical response function reconstruction by interferometric frequency resolved optical gating. Nano Lett. **10**, 2519–2524 (2010)
79. S. Berweger, J.M. Atkin, X.G. Xu, R.L. Olmon, M.B. Raschke, Femtosecond nanofocusing with full optical waveform control. Nano Lett. **11**, 4309–4313 (2011)
80. W. Luo et al., Ultrafast nanoimaging of electronic coherence of monolayer WSe_2. Nano Lett. **23**, 1767–1773 (2023)
81. V. Kravtsov, R. Ulbricht, J.M. Atkin, M.B. Raschke, Plasmonic nanofocused four-wave mixing for femtosecond near-field imaging. Nat. Nanotechnol. **11**, 459–464 (2016)
82. T. Jiang, V. Kravtsov, M. Tokman, A. Belyanin, M.B. Raschke, Ultrafast coherent nonlinear nanooptics and nanoimaging of graphene. Nat. Nanotechnol. **14**, 838–843 (2019)
83. K. Tomita, Y. Kojima, F. Kannari, Selective coherent anti-stokes Raman scattering microscopy employing dual-wavelength nanofocused ultrafast plasmon pulses. Nano Lett. **18**, 1366–1372 (2018)
84. M. Wagner et al., Ultrafast and nanoscale plasmonic phenomena in exfoliated graphene revealed by infrared pump-probe nanoscopy. Nano Lett. **14**, 894–900 (2014)
85. E. Yoxall et al., Direct observation of ultraslow hyperbolic polariton propagation with negative phase velocity. Nat. Photonics **9**, 674–678 (2015)
86. G. Ni et al., Ultrafast optical switching of infrared plasmon polaritons in high-mobility graphene. Nat. Photonics **10**, 244–247 (2016)
87. M. Mrejen, L. Yadgarov, A. Levanon, H. Suchowski, Transient exciton-polariton dynamics in WSe_2 by ultrafast near-field imaging. Sci. Adv. **5**, eaat9618 (2019)
88. A.J. Sternbach et al., Femtosecond exciton dynamics in WSe_2 optical waveguides. Nat. Commun. **11**, 3567 (2020)
89. M.A. Huber et al., Femtosecond photo-switching of interface polaritons in black phosphorus heterostructures. Nat. Nanotechnol. **12**, 207–211 (2017)
90. R. Fu et al., Manipulating hyperbolic transient plasmons in a layered semiconductor. Nat. Commun. **15**, 709 (2024)
91. A. Sternbach et al., Programmable hyperbolic polaritons in van der Waals semiconductors. Science **371**, 617–620 (2021)
92. X. Zhang et al., Ultrafast anisotropic dynamics of hyperbolic nanolight pulse propagation. Sci. Adv. **9**, eadi4407 (2023)
93. J. Nishida, A.H. Alfaifi, T.P. Gray, S.E. Shaheen, M.B. Raschke, Heterogeneous cation-lattice interaction and dynamics in triple-cation perovskites revealed by infrared vibrational nanoscopy. ACS Energy Lett. **5**, 1636–1643 (2020)
94. J. Nishida et al., Nanoscale heterogeneity of ultrafast many-body carrier dynamics in triple cation perovskites. Nat. Commun. **13**, 6582 (2022)
95. J. Nishida et al., Ultrafast infrared nano-imaging of far-from-equilibrium carrier and vibrational dynamics. Nat. Commun. **13**, 1083 (2022)
96. J.M. Atkin, S. Berweger, A.C. Jones, M.B. Raschke, Nano-optical imaging and spectroscopy of order, phases, and domains in complex solids. Adv. Phys. **61**, 745–842 (2012)
97. B.T. O'Callahan et al., Inhomogeneity of the ultrafast insulator-to-metal transition dynamics of VO_2. Nat. Commun. **6**, 6849 (2015)
98. A.J. Sternbach et al., Nanotextured dynamics of a light-induced phase transition in VO_2. Nano Lett. **21**, 9052–9060 (2021)
99. M. Xue et al., Observation and ultrafast dynamics of inter-sub-band transition in InAs twinning superlattice nanowires. Adv. Mater. **32**, 2004120 (2020)
100. M. Xue, D. Pan, J. Zhao, J. Chen, Optically tunable transient plasmons in InSb nanowires. Adv. Mater. **35**, 2208952 (2023)
101. J. Li et al., Ultrafast optical nanoscopy of carrier dynamics in silicon nanowires. Nano Lett. **23**, 1445–1450 (2023)
102. S. Wang et al., Nonlinear Luttinger liquid plasmons in semiconducting single-walled carbon nanotubes. Nat. Mater. **19**, 986–991 (2020)
103. R. Hillenbrand, F. Keilmann, Complex optical constants on a subwavelength scale. Phys. Rev. Lett. **85**, 3029 (2000)
104. N. Ocelic, A. Huber, R. Hillenbrand, Pseudoheterodyne detection for background-free near-field spectroscopy. Appl. Phys. Lett. **89**, 101124 (2006)
105. K. Moon et al., Subsurface nanoimaging by broadband terahertz pulse near-field microscopy. Nano Lett. **15**, 549–552 (2015)
106. J. Zhang et al., Terahertz nanoimaging of graphene. ACS Photonics **5**, 2645–2651 (2018)
107. R. Jing et al., Phase-resolved terahertz nanoimaging of WTe_2 microcrystals. Phys. Rev. B **107**, 155413 (2023)
108. A. Sternbach et al., Inhomogeneous photosusceptibility of VO_2 films at the nanoscale. Phys. Rev. Lett. **132**, 186903 (2024)
109. M.A. Huber et al., Ultrafast mid-infrared nanoscopy of strained vanadium dioxide nanobeams. Nano Lett. **16**, 1421–1427 (2016)
110. M. Plankl et al., Subcycle contact-free nanoscopy of ultrafast interlayer transport in atomically thin heterostructures. Nat. Photonics **15**, 594–600 (2021)
111. T. Siday et al., Ultrafast nanoscopy of high-density exciton phases in WSe_2. Nano Lett. **22**, 2561–2568 (2022)
112. E.Y. Ma et al., Recording interfacial currents on the subnanometer length and femtosecond time scale by terahertz emission. Sci. Adv. **5**, eaau0073 (2019)
113. Z. Fei et al., Gate-tuning of graphene plasmons revealed by infrared nano-imaging. Nature **487**, 82–85 (2012)
114. J. Chen et al., Optical nano-imaging of gate-tunable graphene plasmons. Nature **487**, 77–81 (2012)
115. H. Hu et al., Doping-driven topological polaritons in graphene/α-MoO_3 heterostructures. Nat. Nanotechnol. **17**, 940–946 (2022)
116. F.L. Ruta et al., Surface plasmons induce topological transition in graphene/α-MoO_3 heterostructures. Nat. Commun. **13**, 3719 (2022)
117. H. Hu et al., Gate-tunable negative refraction of mid-infrared polaritons. Science **379**, 558–561 (2023)
118. T. Zhang et al., Spatiotemporal beating and vortices of van der Waals hyperbolic polaritons. Proc. Natl. Acad. Sci. **121**, e2319465121 (2024)
119. F. Guan et al., Compensating losses in polariton propagation with synthesized complex frequency excitation. Nat. Mater. **23**, 506–511 (2024)
120. F. Guan et al., Overcoming losses in superlenses with synthetic waves of complex frequency. Science **381**, 766–771 (2023)
121. K. Zeng et al., Synthesized complex-frequency excitation for ultrasensitive molecular sensing. eLight **4**, 1 (2024)
122. J. Duan et al., Multiple and spectrally robust photonic magic angles in reconfigurable α-MoO_3 trilayers. Nat. Mater. **22**, 867–872 (2023)
123. A.J. Sternbach et al., Artifact free time resolved near-field spectroscopy. Opt. Expr. **25**, 28589–28611 (2017)
124. M. Wagner et al., Ultrafast dynamics of surface plasmons in InAs by time-resolved infrared nanospectroscopy. Nano Lett. **14**, 4529–4534 (2014)
125. A. Charnukha et al., Ultrafast nonlocal collective dynamics of Kane plasmon-polaritons in a narrow-gap semiconductor. Sci. Adv. **5**, eaau9956 (2019)
126. M. Eisele et al., Ultrafast multi-terahertz nano-spectroscopy with sub-cycle temporal resolution. Nat. Photonics **8**, 841–845 (2014)
127. M. Zizlsperger et al., In situ nanoscopy of single-grain nanomorphology and ultrafast carrier dynamics in metal halide perovskites. Nat. Photonics **18**, 975–981 (2024)
128. A.J. Babadjanyan, N.L. Margaryan, K.V. Nerkararyan, Superfocusing of surface polaritons in the conical structure. J. Appl. Phys. **87**, 3785–3788 (2000)
129. M.I. Stockman, Nanofocusing of optical energy in tapered plasmonic waveguides. Phys. Rev. Lett. **93**, 137404 (2004)
130. L. Long, Q. Deng, R. Huang, J. Li, Z.-Y. Li, 3D printing of plasmonic nanofocusing tip enabling high resolution, high throughput and high contrast optical near-field imaging. Light Sci. Appl. **12**, 219 (2023)
131. V. Kravtsov, J.M. Atkin, M.B. Raschke, Group delay and dispersion in adiabatic plasmonic nanofocusing. Opt. Lett. **38**, 1322–1324 (2013)
132. S. Berweger, J.M. Atkin, R.L. Olmon, M.B. Raschke, Light on the tip of a needle: Plasmonic nanofocusing for spectroscopy on the nanoscale. J. Phys. Chem. Lett. **3**, 945–952 (2012)

133. C. Ropers et al., Grating-coupling of surface plasmons onto metallic tips: a nanoconfined light source. Nano Lett. **7**, 2784–2788 (2007)
134. S. Schmidt et al., Adiabatic nanofocusing on ultrasmooth single-crystalline gold tapers creates a 10-nm-sized light source with few-cycle time resolution. ACS Nano **6**, 6040–6048 (2012)
135. K. Toma, Y. Masaki, M. Kusaba, K. Hirosawa, F. Kannari, Control of grating coupled ultrafast surface plasmon pulse and its nonlinear emission by shaping femtosecond laser pulse. J. Appl. Phys. **118**, 103102 (2015)
136. C. Neacsu, G. Reider, M. Raschke, Second-harmonic generation from nanoscopic metal tips: symmetry selection rules for single asymmetric nanostructures. Phys. Rev. B **71**, 201402 (2005)
137. C.C. Neacsu et al., Near-field localization in plasmonic superfocusing: a nanoemitter on a tip. Nano Lett. **10**, 592–596 (2010)
138. D. Sadiq et al., Adiabatic nanofocusing scattering-type optical nanoscopy of individual gold nanoparticles. Nano Lett. **11**, 1609–1613 (2011)
139. S.F. Becker et al., Gap-plasmon-enhanced nanofocusing near-field microscopy. ACS Photonics **3**, 223–232 (2016)
140. F. De Angelis et al., Nanoscale chemical mapping using three-dimensional adiabatic compression of surface plasmon polaritons. Nat. Nanotechnol. **5**, 67–72 (2010)
141. S. Berweger, J.M. Atkin, R.L. Olmon, M.B. Raschke, Adiabatic tip-plasmon focusing for nano-Raman spectroscopy. J. Phys. Chem. Lett. **1**, 3427–3432 (2010)
142. A. Giugni et al., Hot-electron nanoscopy using adiabatic compression of surface plasmons. Nat. Nanotechnol. **8**, 845–852 (2013)
143. M. Esmann et al., Vectorial near-field coupling. Nat. Nanotechnol. **14**, 698–704 (2019)
144. T. Umakoshi, M. Tanaka, Y. Saito, P. Verma, White nanolight source for optical nanoimaging. Sci. Adv. **6**, eaba4179 (2020)
145. J. Vogelsang et al., Ultrafast electron emission from a sharp metal nanotaper driven by adiabatic nanofocusing of surface plasmons. Nano Lett. **15**, 4685–4691 (2015)
146. M. Müller, V. Kravtsov, A. Paarmann, M.B. Raschke, R. Ernstorfer, Nanofocused plasmon-driven sub-10 fs electron point source. ACS Photonics **3**, 611–619 (2016)
147. M. Esmann et al., Plasmonic nanofocusing spectral interferometry. Nanophotonics **9**, 491–508 (2020)
148. K. Tomita, T. Matsuda, F. Kannari, Reduction of graphene oxide by nanofocused ultrafast surface plasmon pulses. OSA Continuum **3**, 2441–2452 (2020)
149. V. Kravtsov et al., Enhanced third-order optical nonlinearity driven by surface-plasmon field gradients. Phys. Rev. Lett. **120**, 203903 (2018)
150. M.A. May et al., Nanocavity clock spectroscopy: resolving competing exciton dynamics in WSe_2/$MoSe_2$ heterobilayers. Nano Lett. **21**, 522–528 (2020)
151. W. Luo et al., Nonlinear nano-imaging of interlayer coupling in 2D graphene-semiconductor heterostructures. Small **20**, 2307345 (2024)
152. E. Quinonez, J. Handali, B. Barwick, Femtosecond photoelectron point projection microscope. Rev. Sci. Instrum. **84**, 103710 (2013)
153. M. Müller, A. Paarmann, R. Ernstorfer, Femtosecond electrons probing currents and atomic structure in nanomaterials. Nat. Commun. **5**, 5292 (2014)
154. G. Hergert, R. Lampe, A. Wöste, C. Lienau, Ultra-nonlinear subcycle photoemission of few-electron states from sharp gold nanotapers. Nano Lett. **24**, 11067–11074 (2024)
155. P. Dienstbier et al., Tracing attosecond electron emission from a nanometric metal tip. Nature **616**, 702–706 (2023)
156. B. Schroeder, M. Sivis, R. Bormann, S. Schaefer, C. Ropers, An ultrafast nanotip electron gun triggered by grating-coupled surface plasmons. Appl. Phys. Lett. **107**, 231105 (2015)
157. J. Vogelsang, G. Hergert, D. Wang, P. Groß, C. Lienau, Observing charge separation in nanoantennas via ultrafast point-projection electron microscopy. Light Sci. Appl. **7**, 55 (2018)
158. G. Hergert et al., Probing transient localized electromagnetic fields using low-energy point-projection electron microscopy. ACS Photonics **8**, 2573–2580 (2021)
159. A. Wöste et al., Ultrafast coupling of optical near fields to low-energy electrons probed in a point-projection microscope. Nano Lett. **23**, 5528–5534 (2023)
160. T.L. Cocker, D. Peller, P. Yu, J. Repp, R. Huber, Tracking the ultrafast motion of a single molecule by femtosecond orbital imaging. Nature **539**, 263–267 (2016)
161. L. Wang, Y. Xia, W. Ho, Atomic-scale quantum sensing based on the ultrafast coherence of an H_2 molecule in an stm cavity. Science **376**, 401–405 (2022)
162. M. Garg et al., Real-space subfemtosecond imaging of quantum electronic coherences in molecules. Nat. Photonics **16**, 196–202 (2022)
163. L.V. Keldysh, Ionization in the field of a strong electromagnetic wave. J. Exp. Theor. Phys. **47**, 1945–1957 (1964)
164. M. Garg, K. Kern, Attosecond coherent manipulation of electrons in tunneling microscopy. Science **367**, 411–415 (2020)
165. S. Grafström, Photoassisted scanning tunneling microscopy. J. Appl. Phys. **91**, 1717–1753 (2002)
166. T.L. Cocker et al., An ultrafast terahertz scanning tunnelling microscope. Nat. Photonics **7**, 620–625 (2013)
167. K. Yoshioka et al., Real-space coherent manipulation of electrons in a single tunnel junction by single-cycle terahertz electric fields. Nat. Photonics **10**, 762–765 (2016)
168. K. Yoshioka et al., Tailoring single-cycle near field in a tunnel junction with carrier-envelope phase-controlled terahertz electric fields. Nano Lett. **18**, 5198–5204 (2018)
169. Y. Terada, S. Yoshida, O. Takeuchi, H. Shigekawa, Real-space imaging of transient carrier dynamics by nanoscale pump-probe microscopy. Nat. Photonics **4**, 869–874 (2010)
170. P. Kloth, M. Wenderoth, From time-resolved atomic-scale imaging of individual donors to their cooperative dynamics. Sci. Adv. **3**, e1601552 (2017)
171. C. Guo et al., Probing nonequilibrium dynamics of photoexcited polarons on a metal-oxide surface with atomic precision. Phys. Rev. Lett. **124**, 206801 (2020)
172. S. Yoshida et al., Terahertz scanning tunneling microscopy for visualizing ultrafast electron motion in nanoscale potential variations. ACS Photonics **8**, 315–323 (2021)
173. V. Jelic et al., Ultrafast terahertz control of extreme tunnel currents through single atoms on a silicon surface. Nat. Phys. **13**, 591–598 (2017)
174. D. Peller et al., Sub-cycle atomic-scale forces coherently control a single-molecule switch. Nature **585**, 58–62 (2020)
175. Y. Arashida et al., Subcycle mid-infrared electric-field-driven scanning tunneling microscopy with a time resolution higher than 30 fs. ACS Photonics **9**, 3156–3164 (2022)
176. C. Roelcke et al., Ultrafast atomic-scale scanning tunnelling spectroscopy of a single vacancy in a monolayer crystal. Nat. Photonics **18**, 595–602 (2024)
177. S. Ammerman et al., Lightwave-driven scanning tunnelling spectroscopy of atomically precise graphene nanoribbons. Nat. Commun. **12**, 6794 (2021)
178. S. Sheng et al., Terahertz spectroscopy of collective charge density wave dynamics at the atomic scale. Nat. Phys. **20**, 1–6 (2024)
179. M. Müller, N. Martín Sabanés, T. Kampfrath, M. Wolf, Phase-resolved detection of ultrabroadband thz pulses inside a scanning tunneling microscope junction. ACS Photonics **7**, 2046–2055 (2020)
180. K. Kimura et al., Terahertz-field-driven scanning tunneling luminescence spectroscopy. ACS Photonics **8**, 982–987 (2021)
181. D. Peller et al., Quantitative sampling of atomic-scale electromagnetic waveforms. Nat. Photonics **15**, 143–147 (2021)
182. V. Jelic et al., Atomic-scale terahertz time-domain spectroscopy. Nat. Photonics **18**, 898–904 (2024)
183. L. Wang, D. Bai, Y. Xia, W. Ho, Electrical manipulation of quantum coherence in a two-level molecular system. Phys. Rev. Lett. **130**, 096201 (2023)
184. O. Takeuchi et al., Probing subpicosecond dynamics using pulsed laser combined scanning tunneling microscopy. Appl. Phys. Lett. **85**, 3268–3270 (2004)
185. H. Mogi et al., Ultrafast nanoscale exciton dynamics via laser-combined scanning tunneling microscopy in atomically thin materials. NPJ 2D Mater Appl **6**, 72 (2022)
186. K. Iwaya et al., Externally-triggerable optical pump-probe scanning tunneling microscopy with a time resolution of tens-picosecond. Sci. Rep. **13**, 818 (2023)

187. S. Yoshida et al., Probing ultrafast spin dynamics with optical pump-probe scanning tunnelling microscopy. Nat. Nanotechnol. **9**, 588–593 (2014)
188. J. Zhu, Ultrafast nano-movie of graphene. Nat. Nanotechnol. **18**, 1263 (2023)
189. Y. Tian et al., Femtosecond-laser-driven wire-guided helical undulator for intense terahertz radiation. Nat. Photonics **11**, 242–246 (2017)
190. R. Jing et al., Terahertz response of monolayer and few-layer WTe_2 at the nanoscale. Nat. Commun. **12**, 5594 (2021)
191. R.H. Kim et al., Terahertz nano-imaging of electronic strip heterogeneity in a Dirac semimetal. ACS Photonics **8**, 1873–1880 (2021)
192. S. Chen et al., Real-space observation of ultraconfined in-plane anisotropic acoustic terahertz plasmon polaritons. Nat. Mater. **22**, 860–866 (2023)
193. M. Obst et al., Terahertz twistoptics-engineering canalized phonon polaritons. ACS Nano **17**, 19313–19322 (2023)
194. S. Labouesse, S.C. Johnson, H.A. Bechtel, M.B. Raschke, R. Piestun, Smart scattering scanning near-field optical microscopy. ACS Photonics **7**, 3346–3352 (2020)
195. X. Chen et al., Hybrid machine learning for scanning near-field optical spectroscopy. ACS Photonics **8**, 2987–2996 (2021)
196. T. Siday et al., All-optical subcycle microscopy on atomic length scales. Nature **629**, 329–334 (2024)